

HST grism spectroscopy of $z \sim 3$ massive quiescent galaxies

Approaching the metamorphosis

C. D'Eugenio¹, E. Daddi¹, R. Gobat², V. Strazzullo^{3,4,5,6}, P. Lustig⁴, I. Delvecchio^{1,5}, S. Jin^{7,8}, A. Cimatti^{9,10}, and M. Onodera^{11,12}

¹ CEA, Irfu, DAp, AIM, Université Paris-Saclay, Université de Paris, CNRS, F-91191 Gif-sur-Yvette, France

² Instituto de Física, Pontificia Universidad Católica de Valparaíso, Casilla 4059, Valparaíso, Chile

³ Faculty of Physics, Ludwig-Maximilians-Universität, Scheinerstr. 1, 81679 Munich, Germany

⁴ University of Trieste, Piazzale Europa, 1, 34127 Trieste TS, Italy

⁵ INAF - Osservatorio Astronomico di Brera, via Brera 28, I-20121, Milano, Italy & via Bianchi 46, I-23807, Merate, Italy

⁶ INAF - Osservatorio Astronomico di Trieste, via Tiepolo 11, I-34131, Trieste, Italy

⁷ Instituto de Astrofísica de Canarias (IAC), E-38205 La Laguna, Tenerife, Spain

⁸ Universidad de La Laguna, Dpto. Astrofísica, E-38206 La Laguna, Tenerife, Spain

⁹ Università di Bologna, Dipartimento di Fisica e Astronomia, Via Gobetti 93/2, I-40129, Bologna, Italy

¹⁰ INAF - Osservatorio Astrofisico di Arcetri, Largo E. Fermi 5, I-50125, Firenze, Italy

¹¹ Subaru Telescope, National Astronomical Observatory of Japan, National Institutes of Natural Sciences, 650 North A'ohoku Place, Hilo, HI 96720, USA

¹² Department of Astronomical Science, SOKENDAI (The Graduate University for Advanced Studies), 650 North A'ohoku Place, Hilo, HI, 96720, USA

Submitted to *A&A*

ABSTRACT

Tracing the emergence of the massive quiescent galaxy (QG) population requires the build-up of reliable quenched samples, disentangling these systems from red, dusty star-forming sources. We present *Hubble Space Telescope* WFC3/G141 grism spectra of 10 quiescent galaxy candidates selected at $2.5 < z < 3.5$ in the COSMOS field. Spectroscopic confirmation for the whole sample is obtained within 1-3 orbits thanks to the presence of strong spectral breaks and Balmer absorption lines. Combining their spectra with optical to near-infrared (near-IR) photometry, star-forming solutions are formally rejected for the entire sample. Broad spectral indices are consistent with the presence of young A-type stars flagging the last major episode of star formation to have taken place no earlier than ~ 300 -800 Myr prior to observation, confirming clues from their post-starburst UVJ colors. Marginalizing over three different slopes of the dust attenuation curve, we obtain short mass-weighted ages and an average peak star formation rate of $\text{SFR} \sim 10^3 \text{ M}_\odot \text{ yr}^{-1}$ at $z_{\text{formation}} \sim 3.5$. Despite mid- and far-IR data being too shallow to determine the obscured SFR on a galaxy-by-galaxy basis, median stack emission from 3GHz data constrains the level of residual obscured SFR to be globally below $50 \text{ M}_\odot \text{ yr}^{-1}$, hence three times below the scatter of the coeval main sequence. Alternatively, the very same radio detection suggests a widespread radio-mode feedback by active galactic nuclei (AGN) four times stronger than in $z \sim 1.8$ massive QGs. This is accompanied by a 30% fraction of X-ray luminous AGN with a black hole accretion rate per unit SFR enhanced by a factor of ~ 30 with respect to similarly massive QGs at lower redshift. The average compact, bulge-dominated morphologies, coupled with the young mass-weighted ages, suggest that the mechanisms responsible for structural transformation might be concomitant with (or preceding) the ones causing quenching.

Key words. Quiescent galaxies – Galaxy evolution – Quenching

1. Introduction

The formation channels that lead to the build up of the red sequence of massive, quiescent galaxies (QGs) that we observe in the local universe are still to be fully understood. In the present-day Universe 75% of the total stellar mass budget is locked into spheroids, either spiral bulges or elliptical galaxies. These are several Gyr-old, pressure-supported stellar systems which are unable to host significant amount of star-formation (Renzini 2006). The majority of massive galaxies ($\log(M_*/M_\odot) > 10.5$) in the local Universe appear to be quenched, with QGs outnumbering star-forming galaxies by a factor of 10 at $\log(M_*/M_\odot) > 11.5$

(Baldry et al. 2004). Fossil records studies have established that the most massive galaxies are the ones where the oldest stellar populations are found, implying an anti-correlation between their stellar mass and the duration of their main star-formation episode (Gallazzi et al. 2005; Thomas et al. 2005; Citro et al. 2016). Such results have then been reinforced by the first identifications of QGs at increasing redshifts (Dunlop et al. 1996; Franx et al. 2003; Cimatti et al. 2004; Daddi et al. 2005) granted by near-infrared (NIR) sensitive detectors which sample the rest-frame optical at $z \geq 1.5$. These advances were essential to show that the assembly and quenching of massive systems took place at $z > 1.5$ with little evolution thereafter of the high-mass end of the luminosity/stellar mass functions, especially compared to the progressive rise of the low-mass end (Fontana et al. 2004;

Send offprint requests to: C. D'Eugenio, e-mail: chiara.deugenio@cea.fr

Cimatti et al. 2006; Arnouts et al. 2007; Drory et al. 2009; Pozzetti et al. 2010; van Dokkum et al. 2014; Gargiulo et al. 2016; Davidzon et al. 2017; Kawinwanichakij et al. 2020). The growth of the lower-mass end of the red sequence can be thought of as the result of the generalized progressive decline of the global star formation rate density through gas consumption, cluster related processes and cosmic starvation affecting the star-forming population mostly at $z < 1.5$ (e.g. Emsellem et al. 2011; Saracco et al. 2011; Carollo et al. 2013; Madau & Dickinson 2014; Sargent et al. 2014; Schreiber et al. 2015; Wild et al. 2016; Maltby et al. 2018; Matharu et al. 2019; Kawinwanichakij et al. 2020). On the other hand, understanding how massive galaxies quenched in an epoch when galaxies were generally gas rich and prodigiously star-forming ($2 < z < 4$, Daddi et al. 2010; Tacconi et al. 2010; Genzel et al. 2010; Madau & Dickinson 2014) is itself non trivial.

Historically, the progressive discovery of populations of massive QGs already in place at high- z (Dunlop et al. 1996; Franx et al. 2003; Cimatti et al. 2004; Daddi et al. 2005; Kriek et al. 2009; Gobat et al. 2012; Glazebrook et al. 2017) posed challenges to hierarchical models of structure formation (e.g. Cimatti et al. 2006; Steinhardt et al. 2016). Hydrodynamical simulations and semi-analytical models (SAM) have struggled to reproduce the comoving number densities of massive, passively evolving galaxies at $z > 2-3$, falling short by roughly an order of magnitude (Wellons et al. 2015; Nelson et al. 2015; Steinhardt et al. 2016; Davé et al. 2016; Cecchi et al. 2019; Schreiber et al. 2018). In recent years, however, confirmations of quiescent galaxies extended up to $z \sim 4$ (Glazebrook et al. 2017; Schreiber et al. 2018; Valentino et al. 2020; Forrest et al. 2020a,b) while cosmological simulations progressively increased in volume, spatial and mass resolution, as well as in improvements of feedback schemes and subgrid physics regulating star formation (Vogelsberger et al. Illustris: 2014a,b; Genel et al. Illustris: 2014; Nelson et al. Illustris: 2015; Pillepich et al. Illustris TNG: 2018; Nelson et al. Illustris TNG: 2019; Schaye et al. EAGLE: 2015; Davé et al. SIMBA: 2019). The most recent estimates of the number density of QGs, either from observational samples or from state-of-the-art cosmological simulations, appear to broadly agree on the number density of quiescent galaxies up to $z \sim 4$ but it is unclear whether a population of passive objects exists as early as $z \sim 5$ in significant numbers (Merlin et al. 2019; Valentino et al. 2020). Additionally, the degree to which such an agreement is robust against systematics, like for example the exact details of sample selection, is not firmly established (Merlin et al. 2019).

Despite the major progress accomplished so far in this field, it remains unclear whether there is a dominant process that causes quenching (Man & Belli 2018). The extreme stellar densities suggested by compact quiescent systems at $z \sim 2$ (Franx et al. 2003; Daddi et al. 2005; van Dokkum et al. 2008; Newman et al. 2012) point at them being remnants of an intense burst of star formation triggered by the rapid collapse of a large amount of gas that occurred at $z > 4$. This could be resulting e.g. from starbursts plunging down into quiescence after dissipative gas-rich mergers (Cimatti et al. 2008; Elbaz et al. 2018; Gómez-Guijarro et al. 2018, 2019; Puglisi et al. 2019) or more “secular-like” evolution through disk instabilities in high-redshift dusty star-forming galaxies, quickly accreting and consuming gas, leaving compact passive remnants (e.g. Dekel et al. (2009); Barro et al. (2013); Toft et al. (2014); Zolotov et al. (2015)). Increased consensus among SAMs and hydrodynamical simulations has been reached when it comes to ascribe the shut down of star formation in massive galaxies to AGN feedback (De Lucia & Blaizot 2007; Henriques et al. 2017; Girelli et al. 2020). Major mergers or vio-

lent disk instabilities can compress the gas into massive compact cores and trigger starburst events which rapidly consume the gas of the system (Dekel & Silk 1986; Murray et al. 2005). Quasar activity is ignited by these processes, launching powerful outflows into the CGM and depleting the host galaxy from its reservoirs (Sanders et al. 1988; Di Matteo et al. 2005; Hopkins et al. 2006; McCarthy et al. 2011). However, AGN feedback is not the only process that can halt or reduce star formation in high- z galaxies. Cosmological starvation (Feldmann & Mayer 2015) and/or the development of a stable virial shock in sufficiently massive haloes (Dekel & Birnboim 2006; Cattaneo et al. 2006) could play a role, followed by maintenance processes such as radio-mode feedback from radiatively inefficient accretion onto a SMBH (Best et al. 2005; Croton et al. 2006), gravitational heating of the diffuse medium from infalling satellites (Dekel & Birnboim 2006; Khochfar & Ostriker 2008; Johansson et al. 2009, 2012) or morphological quenching (Martig et al. 2009). Therefore the detailed study of large, statistically relevant samples of massive quiescent galaxies is crucial to discern among these mechanisms. Robust samples of quiescent galaxies however are challenging to build up: the spectra necessary to reject low redshift interlopers or star forming contaminants become increasingly more difficult to obtain at $z > 1.4$ since it requires either long integrations in 8-10m class ground-based telescopes or space-based observations. Moreover, the rapid drop in number density of massive quenched objects at $z > 1.5$ requires large areas covered by deep observations. On a positive note, on the other hand, one can leverage the boundedness of the age of the Universe to investigate the demographics of the quiescent population across cosmic time as it keeps emerging. In fact, as the population becomes younger and younger at increasing redshift, the discerning power of rest-frame optical spectra at mapping the early star formation of massive QGs surpasses the one at low redshift. This is because around $z \gtrsim 2$ the Universe starts to be young enough to make stellar age differences of ~ 1 Gyr, down to few hundred Myr, visible thanks to the rapid appearance of Balmer absorption lines in stellar populations of ages < 1 Gyr, when A-type stars enter the Turn-Off (therefore increasingly dominating the integrated stellar spectra). Relatively large samples of QGs have been constructed up to $z \sim 2.5$ in COSMOS and the CANDELS fields exploiting large telescopes (e.g. Bezanson et al. (2013); Belli et al. (2015); Onodera et al. (2015); Belli et al. (2019); Kriek et al. (2016); Stockmann et al. (2020)) or HST in combination with strong lensing (Whitaker et al. 2012, 2013; Newman et al. 2018). These studies have been tracing the progressive youngening of $\log(M_*/M_\odot) > 11$ QGs with look-back time, revealing an increasing spread in stellar age and dust extinction with bulk values around 1–2 Gyr and $A_V = 0-1.0$ mag at $z \sim 2$, respectively. This is apparently happening while keeping high metallicities and velocity dispersions ($\sigma = 300-500$ km s $^{-1}$), consistent with local scaling relations (Toft et al. 2012; Onodera et al. 2012; van de Sande et al. 2013; Belli et al. 2015; Kriek et al. 2016; Belli et al. 2017; Estrada-Carpenter et al. 2019, 2020; Stockmann et al. 2020). The progressive appearance of the quenched population can be therefore quantified through the relative fraction of young versus old systems once an age threshold is defined (e.g. age > 1 Gyr, Whitaker et al. 2013). At even higher redshifts, the color selections generally applied to photometric samples already point at a substantial migration of QGs towards bluer colors (Whitaker et al. 2011; Muzzin et al. 2013), accompanied by the drop by roughly one order of magnitude of their number densities (Straatman et al. 2014; Davidzon et al. 2017). Spectroscopic follow-ups have the advantage of refining such picture by testing the colors of selected galaxies against

photometric errors, star forming interlopers or AGN interfering with their spectral energy distribution (SED). Here we present one of the largest samples of spectroscopically confirmed QGs at $2.4 < z < 3.3$ obtained with HST dedicated observations. In section 2 we describe the sample selection. In section 3 we give details on the observational strategy and data reduction. In section 4 we present the spectral analysis and the spectroscopic confirmation of our targets. Section 5 presents their formal classification, the impact of adding COSMOS2015 photometry with or without calibration of zero-points, as well as the use of marginalizing over multiple attenuation laws. In section 7 we constrain their recent star formation history (SFH) comparing the relative strength of the Balmer and 4000Å breaks. In section 8 we investigate the incidence of AGN in our sample. In section 9 we discuss our results in the context of the current literature. Finally, in section 10 we summarize our results and conclusions. We assume a Λ CDM cosmology with $H_0 = 70 \text{ km s}^{-1} \text{ Mpc}^{-1}$, $\Omega_M = 0.27$, $\Omega_\Lambda = 0.73$ and a Salpeter (1955) Initial Mass Function (IMF) unless otherwise specified. Magnitudes are given in the AB photometric system.

2. Sample selection

Given the expected low number density of high- z massive quiescent galaxies, large fields with deep photometric coverage are required for identification and robust assessment of their SEDs. For this reason, we identified a parent sample of more than 50 reliable passively evolving candidates in the 2deg^2 COSMOS field. Sources with $K_{\text{tot}} < 22.5$ were extracted from the McCracken et al. (2010) catalog, limiting the selection to those satisfying the observed-frame BzK color criterion for passive systems (Daddi et al. 2004). Targets formally classified as star-forming BzK with signal-to-noise ratio $S/N < 5$ in the B and z bands were retained, as these photometric candidates are degenerate with quiescent galaxies becoming fainter in such bands with increasing redshift and decreasing mass. Photometric redshifts specifically calibrated for high- z QGs were derived with EAZY (Brammer et al. 2008) as in Onodera et al. (2012) and Strazzullo et al. (2015), adopting the sample of 34 spectroscopically confirmed passive galaxies at $1.3 < z_{\text{spec}} < 2.1$ observed with VLT/VIMOS which later appeared in Gobat et al. (2017) and the sample of 18 passive galaxies at $1.4 < z_{\text{spec}} < 1.9$ of Onodera et al. (2012) observed with Subaru/MOIRCS as calibration samples. Such calibrated z_{phot} were used to select galaxies within $2.5 \leq z_{\text{phot}} \leq 3.5$ and to remove objects with UVJ rest-frame colors inconsistent with passive evolution (Pozzetti & Mannucci 2000; Labbé et al. 2005; Williams et al. 2009). SED fitting was performed using FAST (Kriek et al. 2009) allowing for constant and delayed exponentially declining SFHs. Optical dust attenuation was left free to vary up to $A_V = 5$ mag assuming a Calzetti et al. (2000) attenuation law. Fits were repeated adopting purely quiescent templates only. All sources with optical-NIR broadband photometry consistent with star-forming solutions were rejected. Contamination from dusty star-forming galaxies was further minimized removing objects with Spitzer/MIPS $24\mu\text{m}$ $S/N \geq 4$ detections in Le Floch et al. (2009) catalog, except for galaxies with high-confidence passive SEDs, indicative of mid-IR emission caused by a central dusty AGN torus. Among the most massive bona fide passive candidates, 10 galaxies were targeted for HST WFC3/IR G141 near-IR¹ observations: 9 with $H_{AB} < 22$ ($M_\star > 1.1 \times 10^{11} M_\odot$) plus 1 robust candidate with $H_{AB} = 22.9$ ($M_\star = 8 \times 10^{10} M_\odot$) as the highest- z candidate.

3. HST WFC3 F160W imaging and G141 grism spectroscopy

Ground-based observations have already confirmed the existence of quiescent galaxies at $z \sim 4$ (Schreiber et al. 2018; Valentino et al. 2020; Forrest et al. 2020a,b). However, in the framework of high- z galaxy evolution, their statistical power is mostly modulated by the time-expensiveness of such campaigns. Also, OH sky emission lines and related background notoriously affect the quality of the spectra, sometimes effectively cutting them in correspondence of spectral regions crucial to estimate stellar ages. Space-based observations, instead, ensure extended and continuous spectral coverage. In our specific case, HST WFC3 G141 slitless spectrograph has a spectral coverage from 1.1 to $1.7 \mu\text{m}$ reaching maximum transmission at $1.45 \mu\text{m}$. This allows access to the Balmer/4000 Å break region for all sources lying in our selected redshift range. In addition, relatively good mean $S/N \sim 15$ over 100 Å at $1.6 \mu\text{m}$ is reached with a relatively low number of orbits for sources brighter than $H_{AB} < 22$. These two aspects allow the build up of statistically relevant samples of spectroscopically confirmed $z \sim 3$ quiescent galaxies in a relatively fast way. The G141 dispersion in the first spectral order is $46.5 \text{ Å pixel}^{-1}$ and $R \sim 130$ for unresolved sources and/or compact objects like those considered in this paper. For resolved sources, the spectral resolution is determined by their morphology, namely their size along the dispersion axis. For these reasons, the selected sources were targeted for HST WFC3 observations including imaging and grism spectroscopy. As this paper focuses mostly on the spectroscopic analysis, we refer to Lustig et al. (2020) for a thorough analysis of their morphology.

3.1. Observing strategy

Observations for program GO 15229 took place from January 11th 2018 to December 2nd 2018. Each pointing was observed from 1 to 3 orbits according to each target H_{AB} magnitude, for a total of 17 orbits (see Table 1). For each target the first orbit was split into a direct F160W exposure (for a total of 984 s) and a grism G141 exposure (for a total of 1498 s) adopting the WFC3-IR-DITHER-LINE-3PT dither pattern. For targets with 2 orbits, the second orbit was also split in two, with total exposure 73 s in F160W and 2496 s in G141 adopting WFC3-IR-DITHER-BLOB dither pattern. The third orbit for ID 4 was a repetition of the second one. The ORIENT was carefully chosen for each target in order to avoid any contamination from neighboring sources.

3.2. Data reduction

The data reduction of direct F160W and grism G141 exposures was performed adopting the pipeline *grizli*, version number *0.7.0-34-g91c9412*². After relative alignment between each direct and grism exposures, absolute astrometric registration was performed providing the pipeline with COSMOS ACS I-band reference catalogs of RA/DEC positions of sources brighter than $I_{AB} < 27$ mag within a radius of $5'$ from each target. Grism sky background subtraction is performed by *grizli* by means of the Master sky images from Brammer et al. (2015) applying a grey correction using the F160W flat-field for the G141 grism. Their residuals are generally of the order of 0.5-1% of the overall background level and are further subtracted removing the column-average of the sky pixels in the grism exposures. During this

¹ Rest-frame near-UV/optical.

² <https://github.com/gbrammer/grizli>

Table 1: Coordinates and orbit details for the targeted galaxies.

ID	ID _{Laigle}	RA	DEC	N _{orbits}	total int. time (s)	
					F160W	G141
1	135730	10:01:39.9790	+01:29:34.49	1	983.8	1497.7
2	137182	10:00:57.3452	+01:29:39.46	1	983.8	1497.7
3	252568	09:57:48.5727	+01:39:57.82	2	1056.7	3993.9
4	361413	10:02:09.700	+01:50:24.30	3	1129.7	6490.1
5	447058	09:59:11.7700	+01:58:32.96	2	1056.7	3993.9
6	478302	09:59:13.123	+02:01:34.15	2	1056.7	3993.9
7	503898	10:01:31.8594	+02:03:58.79	1	983.8	1497.7
8	575436	10:00:43.7668	+02:10:28.71	2	1056.7	3993.9
9	707962	09:59:32.5170	+02:22:21.99	1	983.8	1497.7
10	977680	10:00:12.6549	+02:47:23.47	2	1056.7	3993.9

phase the pipeline also runs *Astrodizzle* to reject cosmic rays, persistence and other artifacts. The final drizzling parameters were kept as default. A segmentation map is produced out of the drizzled and combined direct exposure. This is later used to identify and model the spectral trace of each object on each of the grism exposures and to generate model contaminants to be subtracted from the target's cutout. The reduced and decontaminated 2D spectra of our targets are presented in Fig. 1 together with their relative F160W cutouts. At this stage, the detector's FOV is parsed and modelled assuming simple linear continua for all objects in the field (brighter than 25 mag). Grizli then refines the modelling of the brightest objects ([16, 24] mag) with a second order polynomial fit, fitting spectra directly after subtracting off the model for contaminants. The 1D spectra were eventually optimally extracted propagating the background coefficients into the beam dimensions in order to remove any further background residuals. The final adopted scale of the extracted 1D spectra is 0.8 in units of the native dispersion of the G141 spectrograph. The field of view (FOV) of the WFC3-IR channel is 136" x 123", effectively enabling the search for serendipitous spectral breaks. Several of them were found in our grism exposures and will be addressed in a future work.

4. Spectroscopic confirmation

In the following sections we give a detailed description of the method used to measure the redshifts, as well as the criteria adopted to establish the nature of our sources. In brief, we first fitted the spectra alone to extract z_{spec} and check the quality of the z_{phot} calibration. Secondly, we added COSMOS2015 photometry from Laigle et al. (2016) to the analysis adopting the newly derived z_{spec} for SED fitting. We tested the performance of the combined fits when dropping the Zero Points (ZP) corrections proposed in Laigle et al. (2016) and when using different dust attenuation laws. Once the best configuration was identified, we tested the quiescence of individual targets on the basis of their rest-frame UV-to-NIR emission. As dust-obscured star formation manifests itself in emission at longer wavelengths, we searched for further constraints from the mid-infrared (MIR), far-infrared (FIR) and radio emission. Lastly, using the combined information from both spectroscopy and photometry, we characterized our targets in terms of mass-weighted age and dust extinction. We attempted also a direct estimation of the relative light-weighted strength of the Balmer and 4000 Å breaks, so as

to check the post-starburst nature of individual sources suggested by their UVJ colors, despite lacking high spectral resolution.

4.1. Fitting setup

The optimally-extracted spectra were fitted with a custom IDL routine that compares the 1D spectra with composite stellar population templates by χ^2 -minimization. Such templates were generated on the fly by combining a grid of Bruzual & Charlot (2003) (hereafter BC03) simple stellar population (SSP) models with a set of parametric SFHs: a constant, an exponentially declining, a delayed exponentially declining and truncated SFH. In the latter, the initial SFR drops to zero after a cutoff time τ_{tr} from the onset of star formation. In standard τ -models however, τ is the e-folding timescale of the SFH. The ratios of t/τ and t/τ_{tr} , when above unity, approximate the description of an SSP. Due to an apparent systematic excessive broadening when adopting the imaging cutouts to estimate the line spread function, the adopted templates were smoothed to the G141 resolution adopting a FWHM computed fitting the stacked absorption lines of each galaxy with the IRAF task *splot*, resulting in relatively good agreement after visual inspection. The variety in SFHs was chosen in order to allow for both passive and dusty star-forming solutions. The routine fits the observed spectra simultaneously with a set of emission lines complexes using standard line ratios (Anders & Fritze-v. Alvensleben 2003) and the SFR–H α calibration of Kennicutt 1998 where the SFR is taken from the model grid (see Gobat et al. 2012 for further details). In Table 2 we list the grid of parameters used for the fit. For redshift identification, the Calzetti et al. (2000) attenuation law was adopted and the stellar metallicity was left free to vary from 0.4 Z_{\odot} to 2.5 Z_{\odot} . The age of templates was constrained to be lower than the age of the Universe at a limiting redshift as described in the following: in order to reduce the computational cost, we fitted the observed spectra through a first pass done from $z=0.01$ to $z=5.0$ with a low resolution redshift grid ($dz=0.01$). The probability of a given redshift was computed comparing the χ^2 difference between the best fitting solution and all other solutions following Avni (1976) to determine the 1σ confidence range. Once the most probable peaks were identified, we narrowed down the redshift grid around the 1σ peaks, allowing for an interval of $\Delta z \sim 0.2$ spanned at $dz=0.001$. This time we limited the template library to the age of the Universe at the lowest most probable redshift. This approach led to the redshift probability distributions showed in the upper panels of Fig. 2.

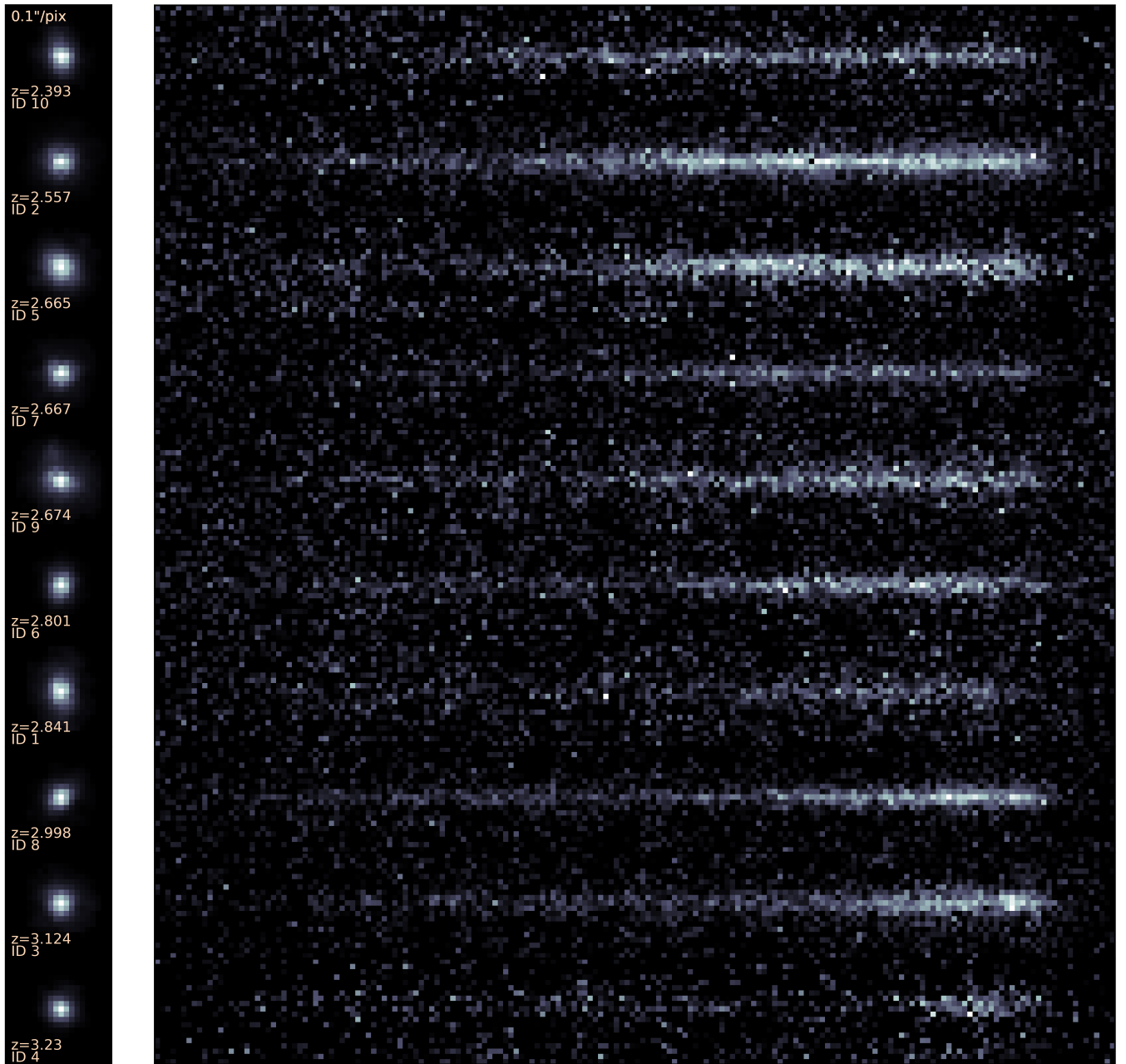


Fig. 1: F160W imaging cutouts (left) and 2D G141 spectra (right) at the native WFC3 pixel scale. Redshift increases from top to bottom. The color scale is in linear scale.

4.2. Redshift identification

Seven of our sources showed unambiguous redshift solutions at a 3σ confidence already during the low resolution pass ($dz=0.01$). Two show a secondary peak within the same confidence level and one (ID 7) lacks a marked spectral break. Nine galaxies out of ten are consistent with single solutions at 1σ . Despite the low resolution of G141 spectroscopy, redshift identification is made possible thanks to the presence of prominent spectral breaks and strong absorption lines for most of the targets (see Fig. 2). For the highest redshift sources, namely ID 3, 4 and 8, MgI and MgII 2640 – 2850 Å absorption lines also enter the spectrograph, albeit with relatively low S/N. Notably, ID 7 lacks absorption features as strong as for the rest of the sample.

This makes the spectrum formally consistent with multiple redshift solutions ($0.4 < z < 3.5$) within 1σ confidence. We checked the consistency of the lowest redshift solutions with the available COSMOS2015 photometry placing $z > 1.5$ as a lower-limit, confirmed by its SED which rises in flux from J to H band. The final spectroscopic confirmation of this source was obtained performing the combined fit of its photometry and grism spectrum across the $1 < z < 3.5$ redshift range at high-resolution ($dz=0.001$). This test confirms the previously derived best fit solution and reduces the error bars on z_{spec} at all confidence levels. At 1σ it yields $z = 2.674^{+0.005}_{-0.009}$, whereas at 3σ it yields $z = 2.674^{+0.021}_{-0.026}$ showing the stability of the best fit solution compared to the information derived from spectroscopy only (see Fig. 2). In the rest of the analysis we will refer to the

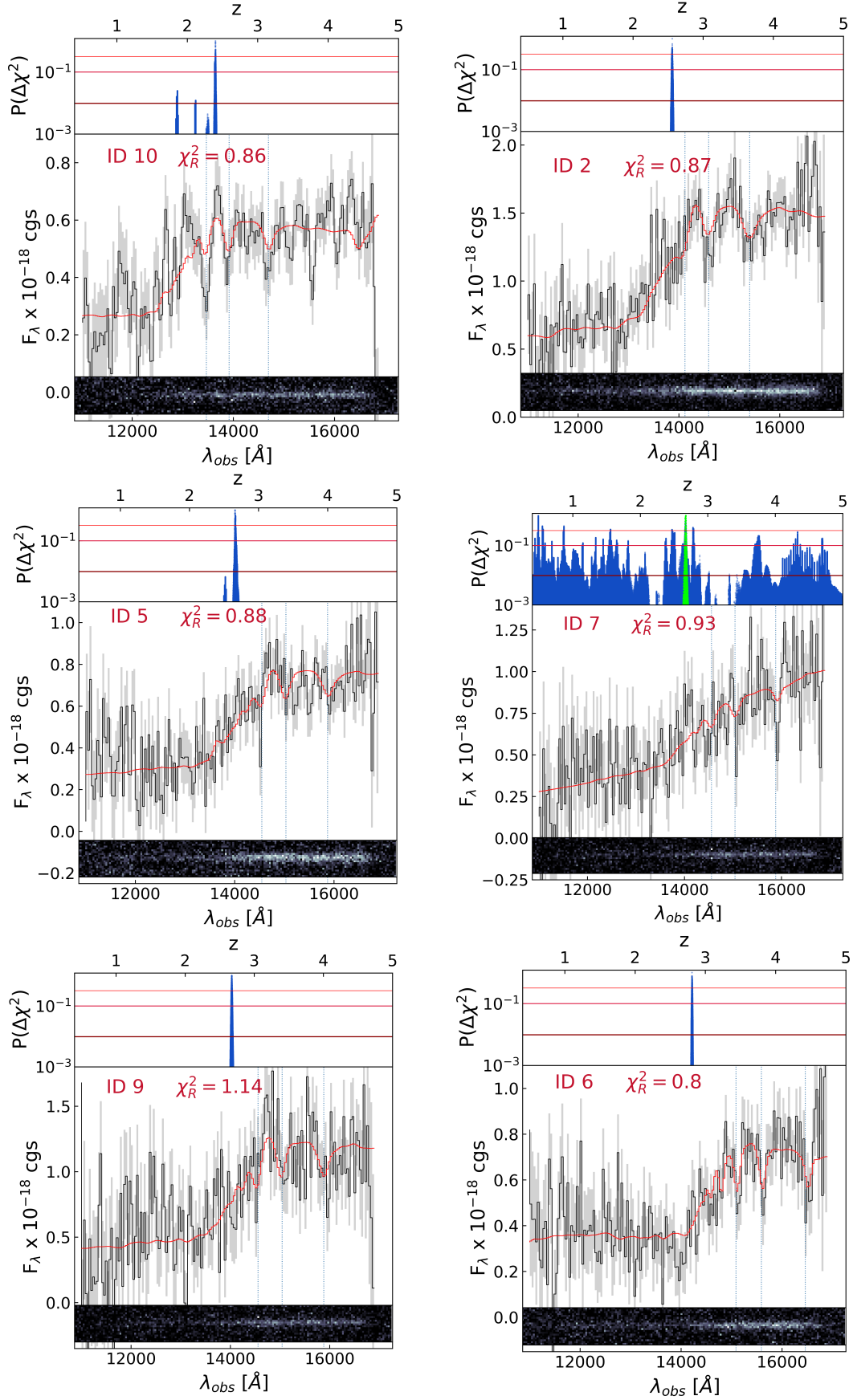


Fig. 2: Upper panels: redshift probability distribution for each target. Solid lines from light- to dark-red mark 1-, 2-, 3- σ confidence levels respectively. Green points for ID7 mark the redshift solutions obtained combining spectroscopy and photometry as described in Sect. 4.2. Middle panels: optimally extracted 1D grism spectra (black) and best-fitting solutions (red) of our targets. The noise vector is showed in grey in each panel. Bottom panels: corresponding 2D G141 spectra. The color scale is in linear scale. Galaxies are shown in order of increasing redshift.

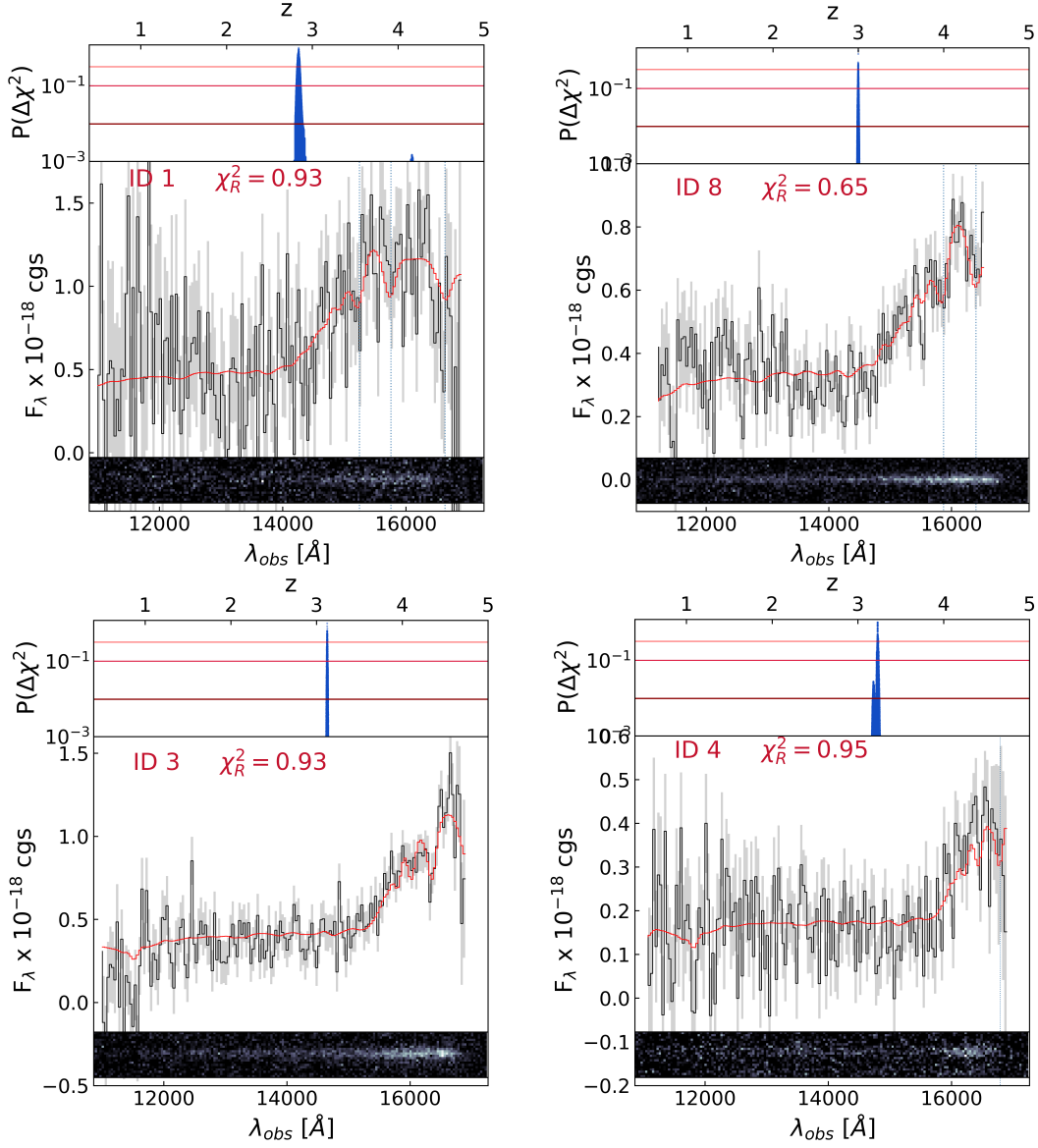


Fig. 2: Continued

Table 2: Grid of parameters used for the spectral fit and the optical-to-NIR SED modeling.

parameter [units]	min	max	step
z	0.01	5	0.01 (then 0.001)
age [Gyr]	0.1	$\text{age}_H(z)$	0.1
τ [Gyr]	0.001	1	0.1
A_V [mag]	0	8	0.1
Z/Z_\odot		0.4, 1, 2.5	
δ attenuation curve (Noll et al. 2009)		-0.7, -0.4, 0 (Calzetti)	
IMF		Salpeter 1955	
Stellar population templates		Bruzual & Charlot 2003	

former confidence level as done for the rest of the sources.

ID 10 shows excess flux at 11870 Å. The secondary peak in the redshift probability distribution is placed at $z=2.3$, where the fitting routine is attempting at reproducing the two most promi-

nent absorption lines with H δ and H γ instead of H ϵ and H δ favored by the best fitting template. This redshift is not low enough to explain the excess flux with a [OII] λ 3727 emission line. Such line would have to be placed at $z=2.18$ yet it would not match with any of the absorption features present in the spectrum. We therefore interpret it as a spurious noise-driven feature.

4.3. Performance of photometric redshifts

We compared the resulting z_{spec} with the calibrated photometric redshifts used for the sample selection to assess the quality of the latter (Fig. 3). The quoted normalized median absolute deviation of the adopted photo- z ³ was $\sigma_{\text{NMAD}} = 0.025$ estimated on the spectroscopically confirmed sample at $z \sim 1.5$, reducing to 0.018 once galaxies with less reliable z_{spec} were excluded. As clarified in Strazzullo et al. 2015, the accuracy is maximum for bright objects (such as those used for spectroscopic confirmation) and decreases for fainter ones (either less massive sources or at higher z). In order to take this into account, in Fig. 3 we show the er-

³ $\sigma_{\text{NMAD}} = 1.48 \cdot \text{median}(|z_{\text{phot}} - z_{\text{spec}}| / (1 + z_{\text{spec}}))$, Hoaglin et al. 1983

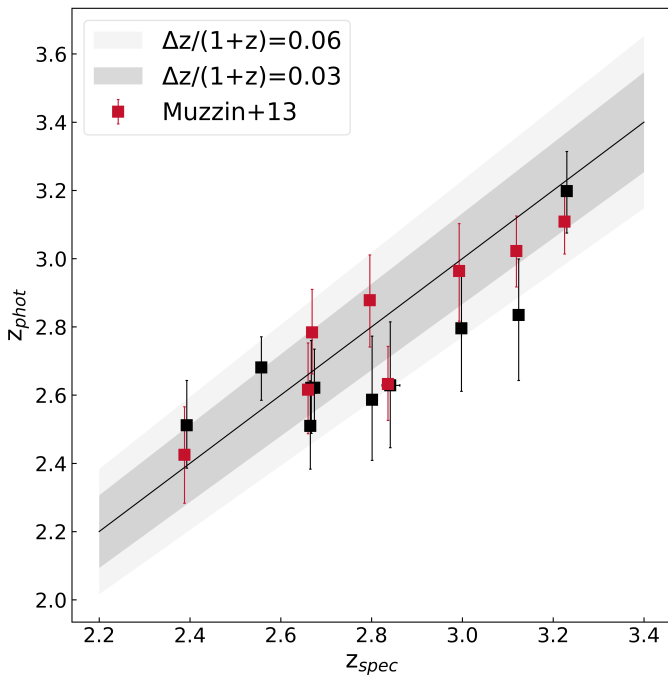


Fig. 3: Comparison between calibrated z_{phot} s and spectroscopic redshifts. Black squares mark the original calibrated z_{phot} s used for the selection. Red squares mark z_{phot} s from Muzzin et al. 2013. The black solid line and relative shaded area mark the 1:1 relation and the nominal dispersions between the original calibrated z_{phot} s and the newly derived z_{spec} (see text). Redshifts from Muzzin et al. 2013 have been shifted horizontally by -0.005 for clarity.

ror bars computed using the z_{phot} accuracy estimated by the authors for faint objects, as a function of the K band magnitude in McCracken et al. 2010. For objects between $K=[20.8, 22]$ - such as in our case - the expected uncertainty is $\sim 0.040(1+z)$. The z_{phot} used for the selection of our sample largely agree with the z_{spec} derived here, with a small systematic underestimation of 0.04%. We included the performance of photometric redshifts from Muzzin et al. 2013 as well. Note that ID 1 and ID 2 are outside the UltraVISTA area and therefore not present in this latter catalog. The nominal σ_{NMAD} we derived here by comparison with our spectroscopic sample are 0.057 and 0.033 respectively for the two catalogs. Applying the same calibration to the Muzzin et al. 2013 photometry at $z \sim 1.5$ (instead of McCracken et al. 2010), the accuracy improved to $\Delta z/(1+z) = 0.015$, especially at $z \geq 1.8$, comparable to that obtained in Muzzin et al. 2013, as can be expected given the deeper photometry in the Muzzin et al. 2013 with respect to McCracken et al. 2010 catalogs (see Strazzullo et al. 2015).

5. Quiescence test: joint spectroscopy and photometry

In order to characterize the physical properties of the targets, the HST grism spectroscopy was combined with COSMOS2015 broadband photometry from CFHT/u* to IRAC/5.8 μm ⁴ (Laigle et al. 2016). A lower limit of 0.05 mag was used for the photometric errors in all the bands. The two data sets were fit

⁴ IRAC/8 μm was excluded from the fit due to higher chances of AGN contamination

separately and later combined by adding the χ^2 matrices of the two fits. This procedure allows to find the solution that best fits both data sets minimizing the impact of residual mismatches in normalization between the spectrum and the photometric SED. The same range of model parameters that was used for the spectral fitting is used in Fig. 4 except for the redshift grid which was fixed to the 1σ range around the best fitting z_{spec} . At this stage, the metallicity was fixed to the solar value according to the normalization and scatter of the local ETG mass-metallicity relation (Thomas et al. 2010). Recent clues from HST/G102 grism spectra of $1 < z < 1.8$ QGs as part of the CLEAR survey seem to support the idea that massive quenched galaxies were enriched to approximately solar metallicity already at $z \sim 3$ (Estrada-Carpenter et al. 2019). As will be mentioned in Sect. 5.3, the results obtained were tested against the choice of template metallicities.

5.1. Photometric zero-point calibrations

When comparing the mass-weighted ages and dust extinction values obtained from the modeling of the grism data alone versus the grism data combined with broad-band photometry (see Sect. 5), we find them being inconsistent at more than 3σ in most cases. Our SED fits to total fluxes resulted in relatively high reduced χ^2 (χ_R^2), as can be seen in Fig. 5. Specifically, the probability associated with the total χ^2 is $\sim 0.5\%$, given the total degrees of freedom of the photometric fit of the whole sample. Changing the IMF or leaving the metallicity of templates free did not improve the χ_R^2 distribution.

As shown in Fig. 6, the means of the distributions of the normalized residuals in each band appear to suffer from systematic shifts, namely B , V , i^+ , z^{++} (marginally), J , H , IRAC/3.6 μm , IRAC/4.5 μm . As noted in Capozzi et al. (2016), the procedure of re-calibrating photometric zero-points (ZPs) to optimize photometric redshift retrieval (commonly performed when building photometric catalogs) can impact the results of SED fitting. These tweaks can introduce systematics in several bands, since the re-calibrations are often based on specific samples at a specific redshift. In the case of COSMOS2015 these were tailored on various samples of spectroscopically confirmed QGs at $z < 2.5$ (Onodera et al. 2012; Krogager et al. 2014; Stockmann et al. 2020), among a much larger number of star-forming galaxies. In addition to this, the templates used to derive such adjustments can also have a role in introducing systematics. In particular, the ones used in COSMOS2015 are: two BC03 templates with an exponentially declining SFH with a timescale $\tau = 0.3$ Gyr and extinction-free templates as in Ilbert et al. (2013); a set of 31 templates including spiral and elliptical galaxies from Polletta et al. (2007) and 12 BC03 templates of young blue star-forming galaxies.

The offsets that we find in our data suggest that model fluxes tend to overestimate observed fluxes when COSMOS2015 ZP corrections subtract flux to the observed signal and viceversa (see Fig. 7). Dropping ZP corrections reduces most of the wavelength-dependent systematics, producing a better agreement between models and the originally observed fluxes. In both Fig. 5 and Fig. 6, it can be seen that dropping ZP offsets has the largest effect compared to changing grid parameters at reducing the median of the χ_R^2 distribution. With this choice the probability associated with the resulting total χ^2 is 9%. A high χ_R^2 could be also flagging systematically low photometric errors. A common practice in such a case is to rescale photometric er-

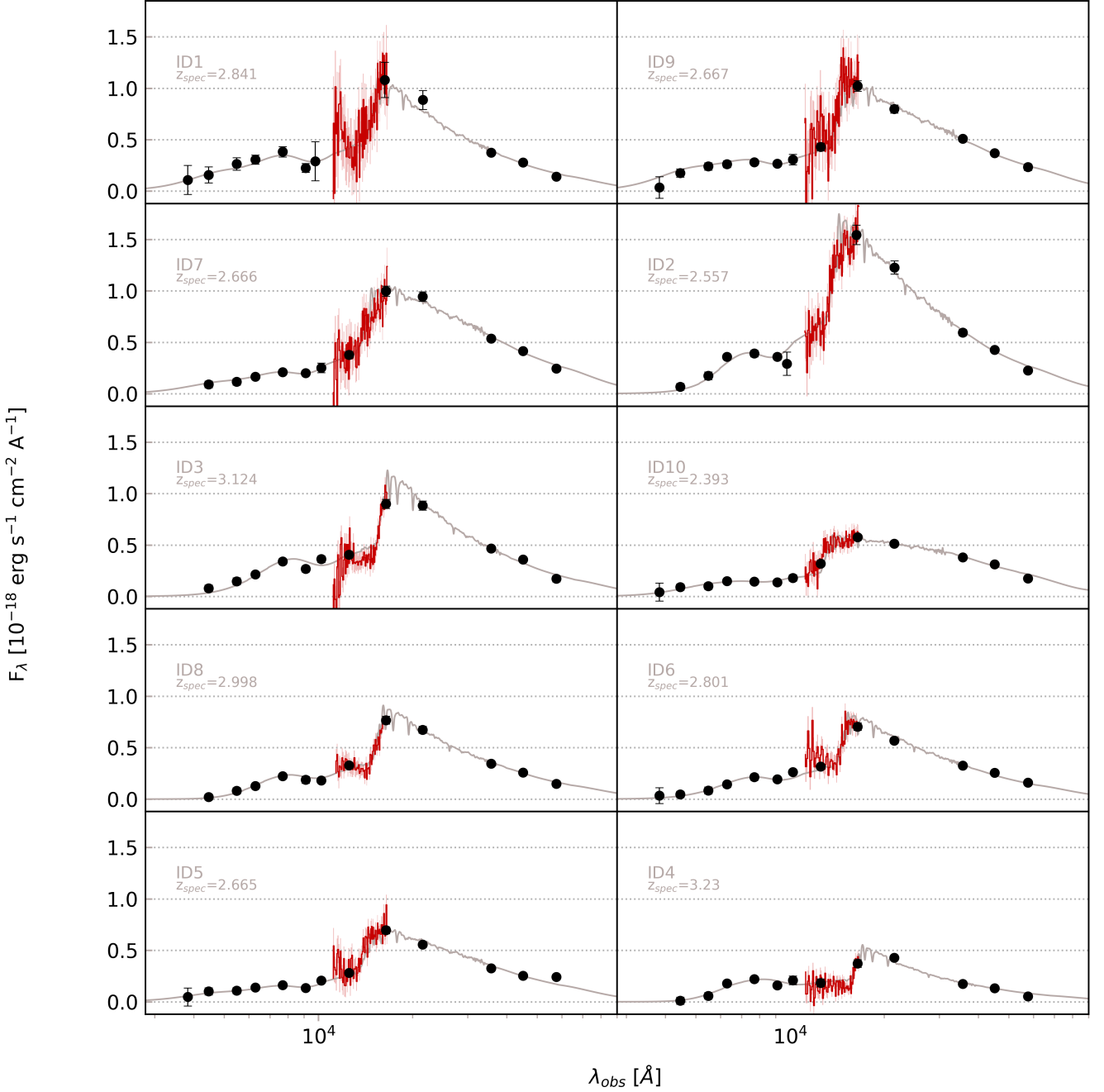


Fig. 4: Photometry from Laigle et al. (2016) catalog (black dots). Grey curves show the best fitting templates smoothed to the G141 resolution. The observed-frame grism spectra are superimposed, rebinned for clarity.

rors to reach a $\chi_R^2 \sim 1$. However, given the behaviour highlighted in Fig. 6 and Fig. 5 such rescaling appears unnecessary. In fact, without using rescaled ZP offsets the median χ_R^2 is very close to 1. Lastly, a high χ_R^2 could be caused by broad residual distributions produced, for example, by the presence of some outliers in the sample. Visual inspections of imaging cutouts relative to each object in each band does not reveal peculiarities. We thus conclude that use of the ZP re-calibrations derived in Laigle et al. (2016) increase the inconsistencies between our spectroscopic and photometric data. For these reasons, the rest of the analysis

has been performed on the original COSMOS2015 photometry, namely without making use of any ZP correction.

5.2. Dust attenuation laws

Once the impact of photometric recalibrations has been reduced, we explored whether any inconsistency in terms of $\Delta\chi^2$ between the best fit spectroscopic solution and the combined one could be ascribed, for example, to an unsuitable attenuation law or to a SFH too smooth to reproduce simultaneously the NUV emission from young stellar populations and the NIR emission aris-

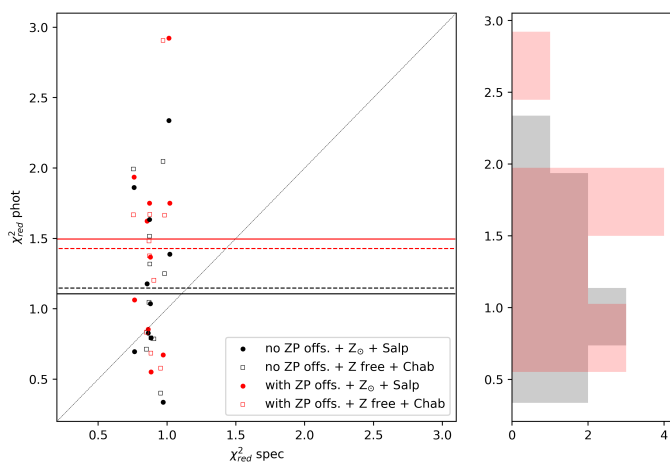


Fig. 5: Distributions of photometric reduced χ^2 before (red dots) and after removing the ZPs re-calibration (black dots). Median values are marked by red and black solid lines respectively. χ_R^2 values obtained adopting a Chabrier IMF and leaving the metallicity free to vary are shown as empty squares. Their corresponding medians are shown as dashed lines.

ing from the bulk of the stellar mass. The use of attenuation laws steeper than Calzetti has been suggested to depend on the SSFRs of galaxies (Kriek & Conroy 2013; Salim et al. 2018). The slope of the curve is generally dependent on the grain size distribution and geometry, with steeper curves associated to differential attenuation according to the age of stellar populations. To test the role of dust attenuation recipes, we included in the fitting library alternative attenuation curves in addition to Calzetti et al. (2000). We adopted the methodology proposed in Salim et al. 2018, following from Noll et al. 2009, where the Calzetti curve is multiplied by a power-law term with exponent δ which sets the slope of the curve itself. Negative δ values imply a steeper slope in A_λ/A_V than in the Calzetti law at rest-frame $\lambda < 5500\text{\AA}$. In this formalism, the Calzetti law has $\delta=0$ by definition, whereas $\delta=-0.4$ is similar to the SMC curve. The curve is further modified by introducing the so-called 2175\AA bump (Fitzpatrick & Massa 1986), modeled as a Drude profile D_λ , with fixed central wavelength and width (FWHM=350 \AA) and varying amplitude. As we linked the bump strength to δ according to the linear relation found by Kriek & Conroy 2013 (see their eq. 3), the law was constrained mainly by one parameter, its slope, which we let vary between 0, -0.4 and -0.7. This latter value was introduced to test the expected behavior of local quiescent galaxies as shown in Salim et al. 2018. One in particular, the curve with $\delta = -0.4$, appears to reduce the dispersion of the χ_R^2 distribution for the photometry and maximizes the consistency of the combined solution with the spectroscopic one. In fact, it systematically yields the lowest $\Delta\chi^2$ (median $\Delta\chi^2=3.1$) between the best fit spectroscopic and combined solutions which makes the two data sets consistent within 2σ , as can be seen in Fig. 8. When testing the overall goodness of fit in terms of the slope, $\delta = -0.4$ is the best fit solution preferred by the majority of the targets. Five galaxies out of nine tend to reject $\delta = -0.7$ at a 5% level (but not at 1%). Given the overall similar goodness of fit (especially between Calzetti and $\delta = -0.4$) it was not possible to reject one of them consistently for the entire sample. Therefore, during the rest of the analysis, we let δ vary, marginalizing over it when deriving physical parameters.

5.3. Quiescence of individual targets

We tested the quiescent/dusty star-forming nature of each galaxy by comparing the goodness-of-fit of the best fitting Constant Star-Forming (CSF) template with a free dust extinction parameter, with that of a solution defined as passive by constraining the best fitting SFH as follows: $t_{50} \geq 0.3$ Gyr, $A_V < 0.8$ mag and $t/\tau \geq 3$ where t_{50} is the lookback time at which the galaxy formed half of its stellar mass (our mass-weighted ages), t is the lookback time at the onset of star formation and τ is the timescale of the SFH. Such ratio corresponds to a drop in SFR of about a factor of 20 with respect to the initial value for an exponentially declining SFH. To classify a galaxy as quiescent, the consistency of the CSF solution has to show a probability of < 0.01 , as inferred from their χ^2 difference. This simple parameterization is able to discern to a zero-order level the consistency of both the spectrum and the photometry with a heavily dust attenuated star forming component, whether it fits better than the passive solution and the confidence level of its consistency. The test was performed fixing the redshift to z_{spec} . We first tested the spectra alone and then combined the photometric information by summing the χ^2 matrices of the two fits. In Fig. 9 we show the results of the test. We verified that letting z_{spec} vary within its 1σ confidence range does not impact the probabilities significantly. Letting the metallicity of the templates vary (adopting 0.4, 1 and 2.5 Z_\odot) has a similarly negligible effect. Once the redshift of the target can be constrained to a sufficient accuracy, the addition of the photometry, with its wide wavelength coverage and overall quality, can help rejecting a SFH in those cases where spectroscopy alone is not able to robustly distinguish between the two. The test on ID 7 was performed letting z_{spec} vary within its 3σ confidence level of the combined fit. Given the lack of prominent (emission or absorption) lines, the spectrum alone is not able to reject star forming solutions. The combined fit, however, rejects such solutions ($P=0$, $\Delta\chi^2=183$, $\chi_{R,\text{SF}}^2=2.0$, $\chi_{R,\text{PASS}}^2=0.9$), even when adopting tighter constraints on the passive solution (e.g. $t/\tau > 10$ and $t > 0.5$). The second object showing the largest consistency with a star forming template is ID 10. Despite the addition of photometry rejecting star forming solutions, it should be noted that this object lies in a region of the UVJ diagram where contamination is expected to be more frequent (see Lustig et al. 2020). Moreover, its best fitting combined mass-weighted age and A_V are still pointing towards a very young and dust reddened stellar content ($t_{50} = 0.3^{+0.3}_{-0.1}$ and $A_V = 1.6^{+0.1}_{-0.3}$, respectively). We discuss very young sources with MIPS and Chandra detections in the following sections. We anticipate here that we consider ID 10 in particular an AGN host and likely an object close to its quenching phase. Given the arguments presented above, we conclude with reasonable confidence that all of our galaxies can be classified as passive on the basis of their UV-to-NIR emission.

6. SFR constraints from multiwavelength data sets

Here we take advantage of the recently released IR to (sub)millimeter Super-deblended catalog of Jin et al. 2018 (hereafter J18) and of the Chandra COSMOS-Legacy Survey catalog of Civano et al. 2016 to estimate the level of obscured star formation or nuclear AGN activity in our targets. First, we convert the flux densities of $24\mu\text{m}$ detections into the SFRs expected from $z \sim 3$ similarly massive MS galaxies and compare them to FIR constraints. Afterwards, we convert the very same flux densities into hard X-ray luminosities to check whether or not they are consistent with being AGN powered. Finally, we derive individual 3σ upper limits on the obscured SFR from VLA 3GHz flux

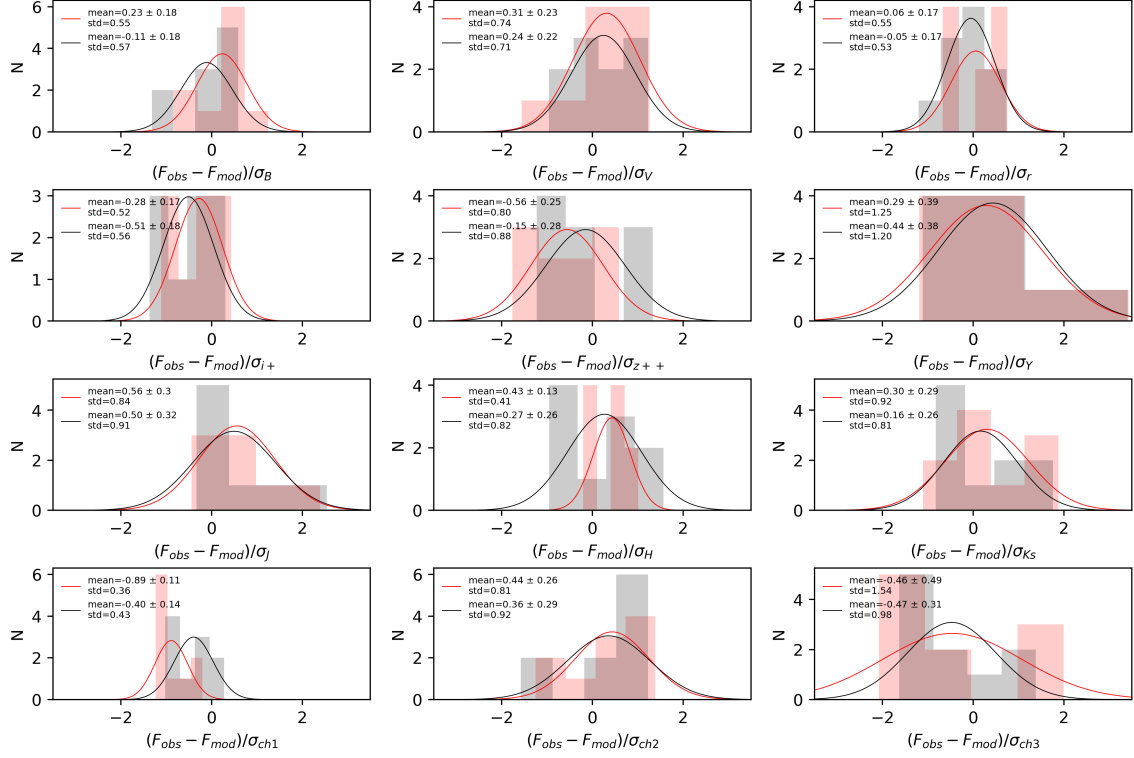


Fig. 6: Normalized residuals distribution of target galaxies in each photometric band. Red and black histograms show residuals adopting re-calibrated and original photometric zero points, respectively. Solid red and black curves show gaussian fits to such distributions. Their means, standard mean errors and standard deviations are listed in each panel.

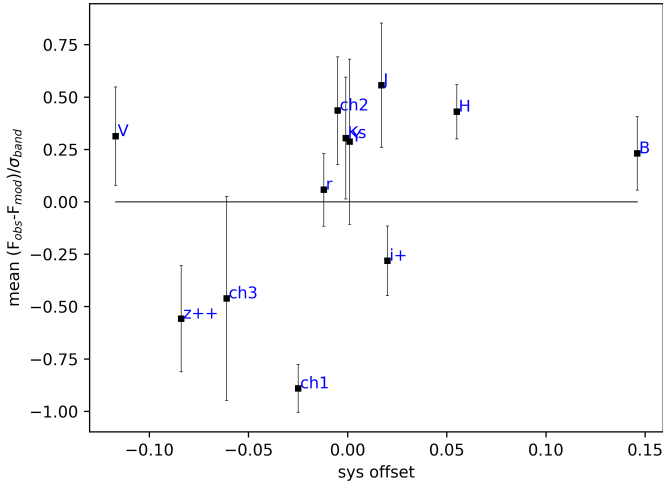


Fig. 7: Mean residuals of photometric bands as a function of the systematic offset to be applied to correct photometric ZPs. A correlation seems to be present, with increasing residuals for increasing corrections. Error bars mark the standard error on the mean shown in Fig. 6.

densities.

The prior-extraction method used in J18 fits the PSF of MIPS 24 μm , VLA 1.4 and 3GHz images (Smolčić et al. 2017) at the positions of known K_S -selected (plus radio 3GHz selected) sources. This procedure improves faint sources identification with respect to blindly-extracted catalogs such as in Le Floch et al. 2009 by

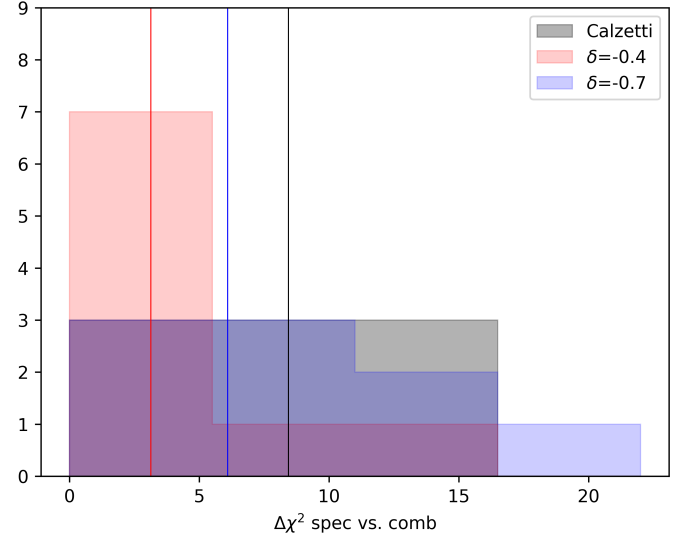


Fig. 8: Chi square difference between the best fitting spectroscopic solution and the best fitting combined solution selected from the spectral χ^2 matrix. Black, red and blue histograms show the distribution of such differences when varying extinction law. Vertical lines mark median values of the distributions. It can be seen that $\delta = -0.4$ is the one that reduces the median offset, bringing the solutions of the two fits consistent within 2σ .

significantly reducing flux errors (by roughly a factor of two) while also improving source deblending. This allows us to in-

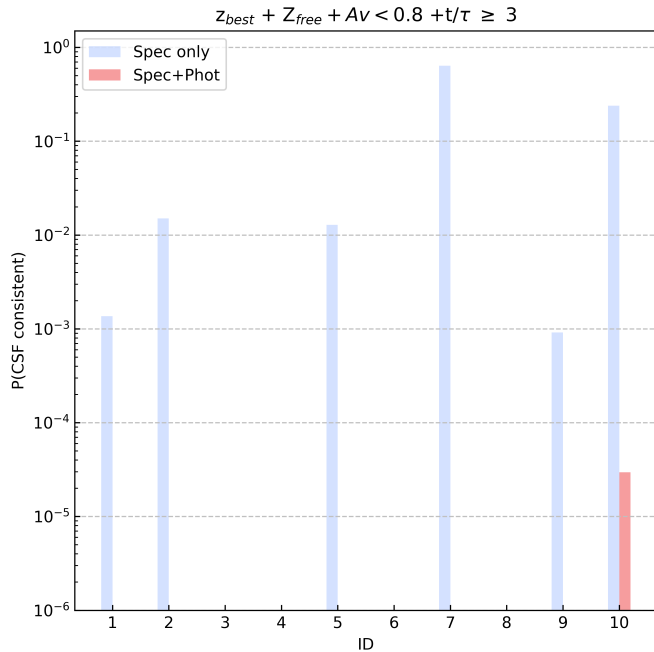


Fig. 9: Probability of constant star forming solutions relative to that of passive solutions. Blue bars mark the results from spectroscopy only. Red bars show the probabilities from the combined fit.

investigate in more detail individual mid- or far-IR detections that could have been missed by previous catalogs or judged of low significance. In particular, we recall here that our sample selection allowed for objects with Spitzer/MIPS $24\mu\text{m}$ detections ($S/N \geq 4$) from the Le Floc'h et al. 2009 catalog, or of higher S/N in case of SEDs with no acceptable star-forming solutions suggestive of an AGN driven MIR flux.

6.1. IR

The Super-deblended catalog marks five of our galaxies as detections in the MIPS $24\mu\text{m}$ band (ID 1, 5, 6, 7 and 10, see Table 3). None of them is significantly detected in the FIR. Specifically, all of them have a $S/N_{\text{FIR+mm}} < 5$, where $S/N_{\text{FIR+mm}}$ is the square root of the quadratic sum of the S/N computed in each band from $100\mu\text{m}$ to 1.2mm . ID 1 formally counts multiple detections in Spitzer/MIPS and *Herschel*/PACS bands but it is flagged as unreliable since it lies in a region of COSMOS affected by incomplete prior coverage and underestimated flux uncertainties. Visual inspection of its MIR and FIR cutouts did not reveal any detection at the source position (see Appendix A). We thus consider the IR detections of ID 1 as unreliable and exclude it from the following test.

At the mean redshift of this sample, observed-frame $24\mu\text{m}$ emission corresponds approximately to $6\mu\text{m}$ rest-frame. Emission at such wavelengths can arise from a range of processes: star-formation (Polycyclic Aromatic Hydrocarbons (PAH) emission lines and/or warm dust continuum); a dusty torus obscuring a central AGN; warm diffuse cirrus clouds heated by old stellar populations or circumstellar dust around Asymptotic Giant Branch (AGB) stars (Draine & Li 2007; Béthermin et al. 2015; Fumagalli et al. 2014). The $\sim 6''$ FWHM of Spitzer/MIPS PSF is larger than the typical optical projected size of our galaxies ($< 1''$ at 5000Å rest-frame) and prevents us from distinguishing

whether the emission is extended or centrally concentrated.

We computed the individual SFRs expected from the remainder four $24\mu\text{m}$ detections under the hypothesis that their emission is powered by star formation at the MS level emitting at the observed flux density. We corrected the flux densities by a factor of 1.7, as recommended in J18 and adopted conversions from Magdis et al. 2012. These conversions were driven from template SEDs of MS galaxies whose variation as a function of redshift is mainly driven by the strength of the mean radiation field $\langle U \rangle$, which maps the sSFR evolution. Such templates assume a fraction of dust mass into PAH of $q_{\text{PAH}} = 2.5\%$ for $z > 1.5$ MS galaxies.

The results can be found in Table 3 where we also report individual 3σ upper limits for undetected sources. The $24\mu\text{m}$ -derived SFRs range between ≈ 300 and $900\text{ M}_{\odot}\text{ yr}^{-1}$. This is the same order of magnitude of $z \sim 3$ $\log(M_{\star}/M_{\odot}) \sim 11$ MS galaxies albeit somewhat higher, inconsistent with FIR non-detections. Such MS galaxies, in fact, typically show FIR *Herschel* flux densities around a few to 10 mJy (Schreiber et al. 2015; Liu et al. 2018; Jin et al. 2018) which would be detected in *Herschel*/SPIRE. ID 10, 6 and 5 appear to tentatively show SPIRE/250- and $350\mu\text{m}$ signal at the source position as revealed by visual inspection. For the latter two, the contamination by nearby projected FIR bright sources due to poor spatial resolution is evident. For ID 10 the J18 catalog formally provides non-detections at 100 and $160\mu\text{m}$ and no deblending at longer wavelengths. In postage stamps, the SPIRE/250 μm signal appears to show emission centered on the source position in the middle between two other $24\mu\text{m}$ bright sources. J18 attribute the 250- and $350\mu\text{m}$ signal to the severe blending of these two sources within the SPIRE large PSF, larger than the distance of these sources from our target ($\approx 10''$). As for the sources that remain individually undetected at $24\mu\text{m}$, the 3σ upper limits are too shallow to reject milder (but substantial) SFRs. Stacking the rest of the sample at $24\mu\text{m}$ results in $0.036 \pm 0.018\text{ mJy}$ which translates into a shallow upper limit of $< 200\text{ M}_{\odot}\text{ yr}^{-1}$. We caution that the available 3σ depth of the Super-deblended data from Spitzer/MIPS, *Herschel*/SPIRE, *Herschel*/PACS in COSMOS is not sufficient to securely reject *sub-MS* levels of obscured star-formation on a galaxy-by-galaxy basis.

6.2. X-rays

ID 10, ID 6 and ID 7 have counterparts in the hard X-ray domain with rest-frame luminosities of the order of $\log(L_{X,2-10\text{keV}}[\text{erg s}^{-1}]) \sim 43.7, 44.3$ and 44.3 respectively, assuming a photon index $\Gamma = 1.4$ (e.g. Gilli et al. 2007). We tested whether their $24\mu\text{m}$ emission is consistent with being powered by an accreting black hole converting the observed-frame $24\mu\text{m}$ flux densities to unobscured rest-frame X-ray ($2-10\text{keV}$) luminosities, adopting the relation of Fiore et al. (2009) (see their eq. 1). This relation assumes that the $2-10\text{ keV}$ luminosity, computed directly from the observed fluxes without any correction for intervening absorption, can be considered representative of the intrinsic X-ray luminosity. The relation has a scatter of 0.2 dex and outliers in the case of significant X-ray absorption. For these three sources, their expected $L(2-10\text{keV})_{24\mu\text{m}}$ are in agreement with the observed ones within the uncertainties (see Table 3). Therefore, although we cannot reject the scenario in which some level of star formation would contribute to the rest-frame $6\mu\text{m}$ emission, we conclude that our data are fully explained by an AGN obscured by a dusty absorber.

Lastly, ID 5 shows a 0.1 mJy $24\mu\text{m}$ detection at 10σ significance which is not matched by an X-ray detection. Given that its spec-

trum and photometry are both pointing towards a passive nature, we tend to favour the hypothesis for which strong obscuration might be playing a role in hiding X-ray photons from the central engine.

6.3. Radio

We derived individual 3σ upper limits on the obscured SFR from the Super-deblended VLA 3GHz flux densities using the FIR-Radio correlation of Delvecchio et al. 2020 assuming that radio emission is given by star formation only. One galaxy is detected at 3GHz at 19σ (ID 1). Given the unphysically high SFR estimated for it ($\sim 10^4 M_\odot \text{ yr}^{-1}$, see Table 3), the origin of its radio emission is to be ascribed to AGN radio jets. Otherwise, the inferred upper limits result in $<120\text{--}190 M_\odot \text{ yr}^{-1}$, which do not conclusively rule out the presence of sub-MS levels of star formation on a galaxy-by-galaxy basis. Finally, as derived in D'Eugenio et al. 2020, the peak flux density of $S_{3\text{GHz}}=2.72\pm0.93 \mu\text{Jy}$ obtained by mean-stacking 3GHz-undetected sources, translates into an upper limit on the global obscured SFR of $\sim 40\text{--}50 M_\odot \text{ yr}^{-1}$, a level of star-formation a factor of 6 lower than the coeval MS.

In summary, the average obscured SFR of our sample has been constrained to be below $\sim 40\text{--}50 M_\odot \text{ yr}^{-1}$ by a mean-stack detection at 3 GHz. However, individual 3 GHz radio upper limits to the obscured SFR are $<120\text{--}190 M_\odot \text{ yr}^{-1}$, therefore not sufficient to reject, on a galaxy-by-galaxy basis, star formation at 1σ below the estimated value for the MS at $z\sim 2.8$ corresponding to our stellar masses. Our sample contains four secure MIPS $24\mu\text{m}$ detections ($f_{24\mu\text{m}} \sim 0.1\text{--}0.2\text{mJy}$) with no FIR counterparts given also the shallow upper limits at these redshifts. Three of these detections are consistent with being AGN-powered given their luminous X-ray counterparts. The combined passive stellar emission for the remaining MIPS source points toward such galaxy being a likely obscured AGN host. The lack of individual strong constraints on the residual obscured SFR at these redshifts, combined with very young mass-weighted ages and high dust extinction values for some of our targets, renders the classification on a galaxy-by-galaxy basis somewhat ambiguous. We argue that extended spectral coverage (e.g. covering $\text{H}\alpha$ and $[\text{NII}]$) could be of help on this matter and that conclusive evidence on the nature of such high- z QGs can be obtained only with targeted deep mm observations.

7. Age determination

7.1. Spectral fit

Recent works suggest that, when it comes to estimating age and optical dust extinction, relatively simple parameterisations of the SFH perform similarly as more flexible ones and, all in all, behave in a relatively stable way at high redshift (Belli et al. 2019; Valentino et al. 2020). We conservatively marginalize over the different SFHs adopted here as to render the best fitting values and their uncertainties more robust. Fig.10 shows the resulting t_{50} and A_V extracted from the grism spectra (blue points) compared to those derived including COSMOS2015 photometry (red points). Light to dark shading marks 3σ , 2σ - and 1σ level confidence values respectively, obtained following Avni (1976) with two interesting parameters. The degeneracy between t_{50} and A_V appears to be strongly mitigated by the addition of the photometry once the redshift is constrained with sufficient accuracy to the

spectroscopic value. The bulk of our targets are consistent with having formed half of their stellar mass relatively recently, systematically having t_{50} below 1 Gyr. In some cases, such as for ID 10 and ID 6, the best fitting combination suggests the presence of dust enshrouded young stellar populations. Intriguingly these two galaxies are also detected in X-rays and $24 \mu\text{m}$, as discussed in sections 6.1 and 6.2, and might be galaxies which just entered into their quiescent phase or with residual SF below the levels probed our FIR data.

7.2. Relative strength of spectral breaks

The choice of SFH to infer evolutionary parameters intrinsically carries a degeneracy with the functional form adopted. A more direct approach is to quantify the light-weighted contribution of recent star-formation by measuring the relative contribution to the integrated stellar spectrum of short-lived massive stars with respect to long-lived lower-mass stars. Balmer absorption lines reach their maximum strength in A-type stars with a spectral break at 3646 \AA . Stars of lower mass and lower effective temperature produce metal absorption lines (Ca H & K, Fe, Mg) which result in a sharp spectral break at 4000 \AA . Moreover, the underlying continuum changes shape with time, progressively losing emission in the NUV/blue spectral range while flattening in the NIR. The different evolutionary rates of the stars producing the lines and their fractional contribution to the optical light at fixed mass, make it possible to trace the evolutionary stage of a galaxy. In Fig 11 (upper panels) we show the evolution of the spectral break measured through the D_B definition (Kriek et al. 2006) and the D_n4000 definition (Balogh et al. 1999) respectively, as well as the relative strength (the ratio) between the two (lower left panel). Lighter shaded curves show the variation with increasing duration of star-formation. The ratio is shown as a function of age of composite templates built with a short truncated SFH. The ratio is only mildly dependent on dust reddening since the two indices share a similar wavelength range. Also, the two indices are fairly robust against low resolution. As can be seen, the ratio varies strongly during the first 1 Gyr or so, reaching its maximum around 0.3-0.5 Gyr. Eventually, it drops below 1 once the light-weighted contribution from A-type stars fades away. Constant star-formation results instead in a ratio of ~ 1.1 rather constant with time. Varying the metallicity of the input templates has the effect of anticipating the transition to $D_B/D_n4000 > 1$. This effect is strongest when adopting supersolar metallicity ($2.5Z_\odot$) when the transition is reached at 0.9 Gyr. We suggest that such ratio could be used to spot post-starburst galaxies with high dust attenuation along and across the UVJ diagram when high-resolution spectra are unavailable.

In Fig. 11 (upper right) we show the two indices computed on our targets. The grey dashed line highlights the transition where the post-starburst ratio equals 1. The mean error in each side band was divided by the square root of the number of pixel within it. For ID 4, whose rest-frame spectrum does not cover the entire wavelength range required to compute the D_n4000 red side-band, the average flux density was taken as the mean of the best-fitting template in the same range. The error was computed as the mean of the noise spectrum taken on the last 10 spectral bins. We flagged this galaxy with a red diamond. The red star marks the values obtained on the average spectrum in D'Eugenio et al. (2020). Despite the large uncertainties driven by the S/N of our spectra, the indices all lie well above the 1:1 relation, thus marking the presence of young stellar populations in all of our targets. This supports the results of the spectral modeling, highlighting

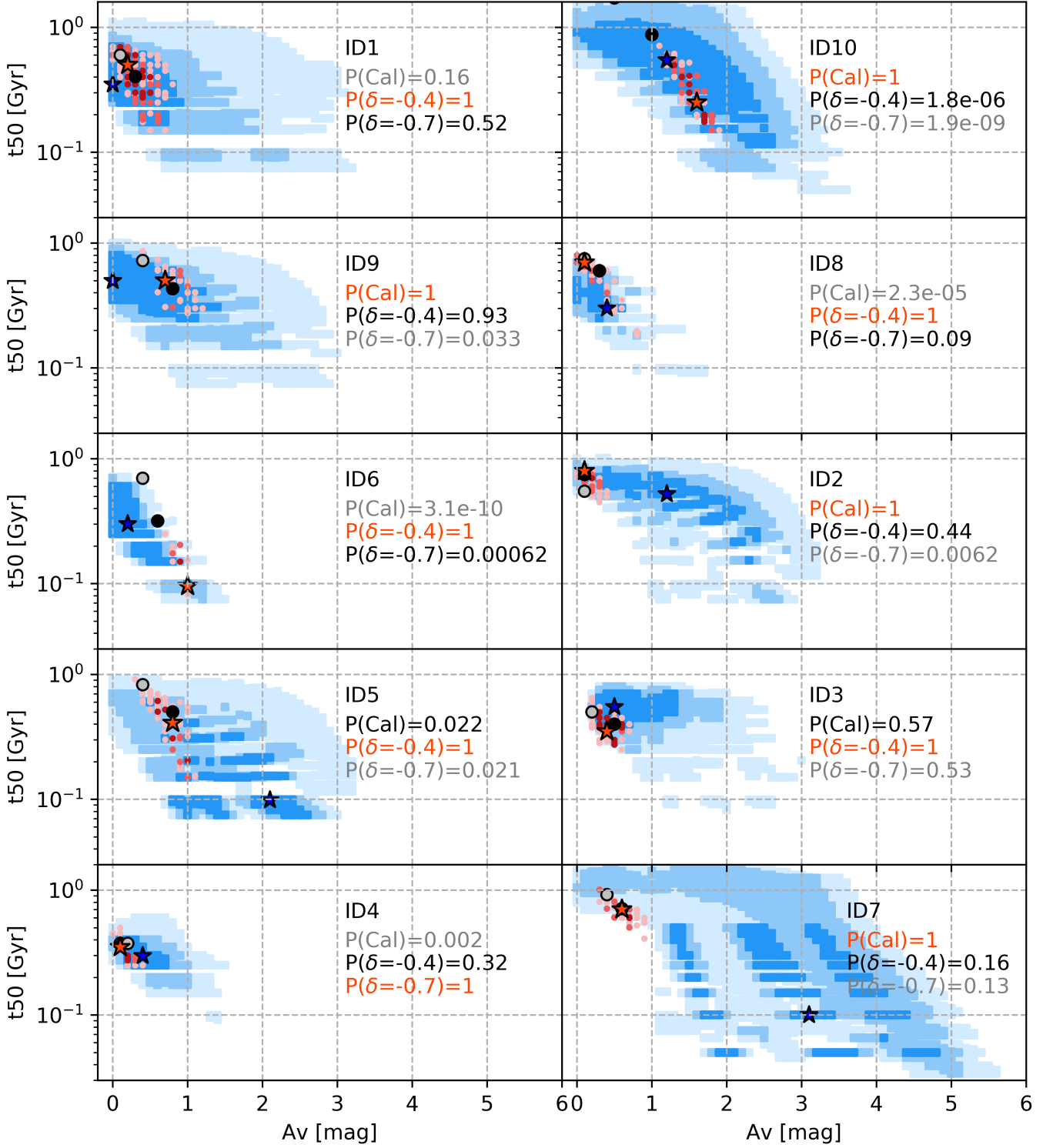


Fig. 10: Mass-weighted ages and dust extinction values for our targets. Blue squares mark the confidence regions (3 to 1 σ going from light to dark points) extracted from the spectra only. Red points show the solutions of the combined fit. Blue and red stars in each panel mark the best fit solution from the spectroscopic fit and the combined fit respectively. The probability of consistency of each extinction law with respect to the best fitting one are reported for each galaxy. As a reference, we report the best fitting combined solution at fixed extinction law as black and grey dots, their color coding follows that of the aforementioned probabilities.

how some of the most massive high- z QGs appear to be only recently quenched (Stockmann et al. 2020; Valentino et al. 2020; Forrest et al. 2020b). An overview of the physical parameters derived for our target galaxies can be found in Table 3.

8. Tracing AGN activity

Here we investigate the incidence and strength of BH activity on newly quiescent galaxies, in the framework of SMBH-galaxy

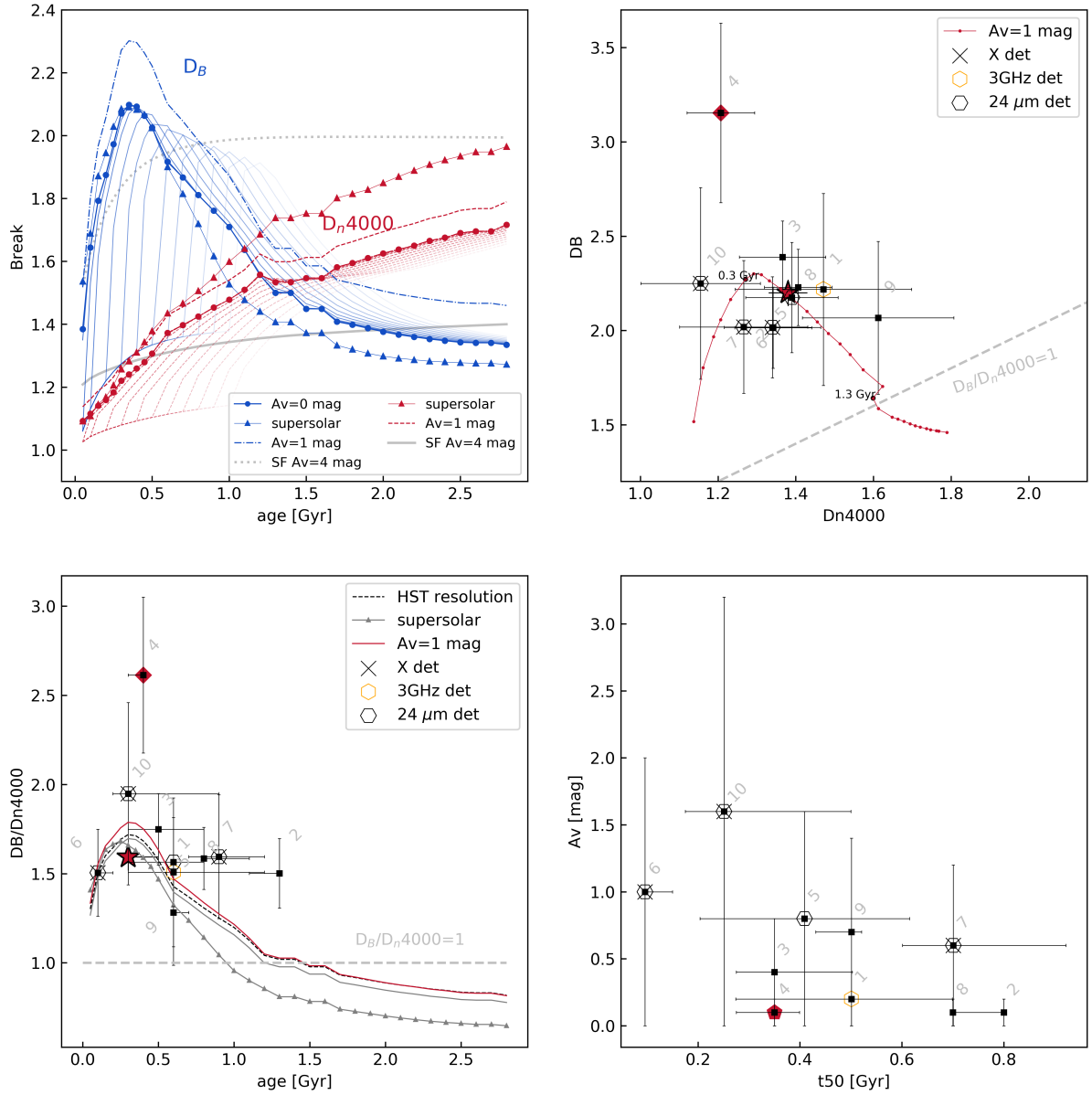


Fig. 11: *Upper left:* variation of the Balmer and 4000 Å breaks for CSPs as a function of their age using BC03 templates at solar metallicity. Lighter curves mark the evolution for a truncated SFH with increasing duration of star formation. The effect of adopting templates of different metallicity is displayed for the values that produce the largest variation, i.e. $2.5Z_{\odot}$ (triangles). Dotted and solid gray curves show the behavior of a constant SFH for the two breaks respectively. *Upper right:* individual values of D_B and D_{n4000} for our targets. The red track shows their evolution with age and is attenuated by 1 mag. The gray dashed line marks the 1:1 relation. *Lower left:* variation of the index ratio as a function of age for an SSP-like template. The effect of smoothing templates to the HST resolution is shown by a black dashed curve. The effect of a $A_V=1$ mag attenuation is shown instead by a red curve. The full transition between a Balmer-dominated and a 4000 Å -dominated spectrum is flagged when $D_B/D_{n4000}=1$ (grey dashed line), which happens around 1.3 Gyr of passive evolution. Dark grey triangles mark the evolution for $2.5Z_{\odot}$ templates. *Lower right:* best-fit values for the dust attenuation and mass-weighted age from the combined fit. Chandra X-ray, VLA 3GHz and Spitzer/MIPS 24 μ m detections are marked by black crosses, yellow and black hexagons respectively.

coevolution. In particular we can assess the level of mechanical feedback on our galaxies by studying the rest-frame 1.4 GHz luminosity averaged over the entire sample; and the incidence of radiatively efficient accretion by constraining the fraction of X-ray detected galaxies and their rest-frame hard X-ray luminosity respectively.

8.1. Radio

As mentioned, one galaxy (ID 1) is securely detected at 3GHz. Given the unphysically high SFR estimated for it ($\sim 10^4 M_{\odot} \text{ yr}^{-1}$), we ascribe the origin of its radio emission to AGN radio jets. Stacking the radio-undetected sources, in D'Eugenio et al. (2020) we obtained a peak flux density of $S_{3\text{GHz}}=2.72\pm0.93 \mu\text{Jy}$.

This translates into a K-corrected rest-frame luminosity of $L(1.4 \text{ GHz}) = (2.0 \pm 0.7) \cdot 10^{23} \text{ W/Hz}$, which we interpret in this section as arising from low-luminosity AGN activity. Under the assumption that $z \sim 2.8$ quiescent galaxies share a FIR-to-radio SED similar to that of $z \sim 1.8$ analogs, we rescaled the best-fit model to the stacked SED of Gobat et al. 2018 (hereafter G18) to our median stellar mass and computed the 1.4 GHz luminosity expected from residual star formation according to the FIR-radio correlation ($L_{\text{mod}} = 1.2 \cdot 10^{22} \text{ W/Hz}$). Our observed $L(1.4 \text{ GHz})$ is 18 times higher, implying an excess signal of $L_{\text{mod}} = 1.8 \cdot 10^{23} \text{ W/Hz}$. This, in turn, is a factor of 3-4 higher than the excess found in $z \sim 1.8$ similarly massive QGs (G18). The low statistics implied by our sample size prevents us from making meaningful considerations on the overall duty cycle of AGN activity. It is worth mentioning, however, that the 0.66 duty cycle estimated in G18 from $z = 1.4$ to $z = 2.5$ implied a burst duration of 1.2 Gyr which is 1.6 times larger than our observational window (the cosmic time spanned by our sample is 0.72 Gyr). This, together with the ensemble radio detection, might imply that we are sampling an epoch when low-level AGN activity is almost always on in newly quiescent galaxies, with a stronger radio AGN activity with respect to what inferred for lower- z massive analogs.

8.2. X-ray

L_X can be viewed as a tracer of the typical rate of black hole growth in a given galaxy sample. Recent stacked analysis of quiescent galaxies in COSMOS constrains the average level of rest-frame hard X-ray emission to be $L_X = 2 \cdot 10^{43} \text{ erg s}^{-1}$ (Carraro et al. 2020, hereafter C20)⁵. While our non-detections are consistent with C20, our mean rest-frame $L(2-10)\text{keV}$ obtained as

$$L(2-10)\text{keV} = \frac{L_{X,\text{uplim}} \times N_{\text{non-det}} + \sum_{i=1}^{N_{\text{det}}} L_{X,i}}{N_{\text{non-det}} + N_{\text{det}}}$$

is higher by a factor of 2–3 at face value (see Fig. 12). The error bar on the average is computed as the error on the weighted mean.

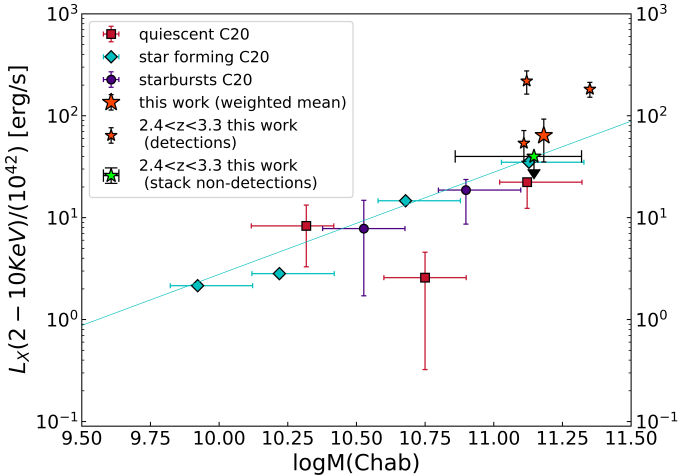


Fig. 12: X-ray luminosity in the 2-10 keV band as a function of stellar mass for quiescent (red squares), star forming (cyan diamonds) and starburst galaxies (violet circles) at $2.25 < z < 3.50$. Adapted from Carraro et al. 2020.

⁵ Our stellar masses were converted to a Chabrier IMF for consistency

Assuming the Lusso et al. (2012) bolometric corrections and a $M_{\text{BH}} = M_{\star}/500$ conversion as in Häring & Rix (2004), we computed Eddington ratios for each target, defined as the bolometric X-ray luminosity (or its 3σ upper limit) divided by the Eddington luminosity expected at the stellar mass of the galaxy. We obtain Eddington ratios of $\lambda_{\text{EDD}} \sim 2 - 11\%$ for detected sources and 3σ upper limits lower than 1% for all the undetected ones. When repeating the test using $24\mu\text{m}$ -derived $L(2-10)\text{keV}$, we obtain λ_{EDD} which are a factor of 2 higher on average. Such λ_{EDD} translate into Black Hole Accretion Rates (BHAR)⁶ which are largely in agreement with C20 at $z \sim 3$. Dividing the mean $\langle \text{BHAR} \rangle$ by the average $\langle \text{SFR}_{[\text{OII}]}\rangle$ estimated in D'Eugenio et al. (2020) we obtain an increase by a factor of ~ 30 with respect to $1.3 < z < 2.25$ QGs at the same mass (see Fig. 13), consistent with the lower limit for massive $2.3 < z < 3.5$ QGs inferred from the same paper. Our mean L_X is marginally consistent with that star-forming galaxies in the same mass and redshift range, whereas the [OII]-derived dereddened SFR lies around ~ 60 times below the MS. This translates into $\langle \text{BHAR} \rangle / \langle \text{SFR} \rangle$ being a factor of ~ 60 higher than the high-mass end of the MS at $z \sim 3$. This supports the idea that, while the stellar mass growth of the host galaxy has already come to an end, the BH mass growth in high- z QGs takes longer to fade away, as already pointed out in C20, and might have had a role in quenching.

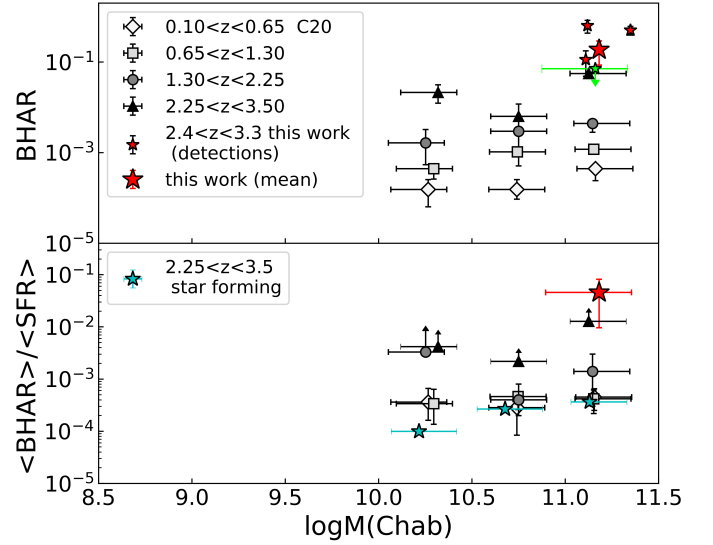


Fig. 13: BHAR (top) and BHAR per unit star formation rate (bottom) as a function of stellar mass for quiescent galaxies in COSMOS. Different symbols mark different redshift bins. Cyan stars mark main sequence galaxies in the same redshift range studied in this work. Error bars on the average BHAR reflect the dispersion of the weighted mean on the rest frame $L(2-10\text{keV})$ of the sample. The average $\text{SFR}_{[\text{OII}]}$ was converted to a Chabrier IMF. Adapted from Carraro et al. (2020).

The stochastic nature of detectable AGN activity implies that it is usually only observed in a small fraction of galaxies at a given time. Aird et al. (2019) report that high- z massive QGs exhibit enhanced AGN fractions compared to low- z SF galaxies hosting an equivalent SFR, suggesting that AGN activity in QGs

⁶ $\text{BHAR}(M_{\star}, z) = (1 - \epsilon) \cdot L_{2-10\text{keV}} \cdot \text{kbol}(M_{\star}, z) / (\epsilon c^2) = \lambda_{\text{EDD}} \cdot L_{\text{EDD}} \cdot 10^{-45.8} M_{\odot} \text{ yr}^{-1}$, where the efficiency of mass conversion is $\epsilon = 0.1$

might be fuelled and sustained by stellar-mass loss rather than the availability of cold gas. Their fraction of highly-accreting quiescent galaxies ($\lambda_{\text{SBHAR}} > 0.1$, i.e. at more than 10% the Eddington limit) reaches 2-3% around $z \sim 3$. The fraction of normally accreting AGN ($\lambda_{\text{SBHAR}} > 0.01$) reaches 20-30% in the quiescent population with SFRs of order of $0.5\text{--}1\text{ M}_{\odot}\text{ yr}^{-1}$.

Schreiber et al. (2018) find 18% of X-ray detections among $3.2 < z < 3.7$ massive UVJ-quiescent galaxies, plus an additional 30% in the young-quiescent (lower-left) region of the UVJ diagram. Several of their young-quiescent SEDs show similarities with our ID 5 and 6 in terms of SED shape and possibly young age. Olsen et al. (2013) report a $19\% \pm 9\%$ luminous AGN fraction in a mass-complete sample of massive UVJ selected quiescent galaxies at $1.5 < z < 2.5$, with a total low-luminosity AGN fraction up to 70%-100%, advocating in favor of episodic AGN activity to maintain low SFRs in quiescent galaxies. Including a possibly Compton thick source, our sample likely contains a 40% fraction of luminous AGN. We currently do not know in which direction the incompleteness due to the sample selection will affect the AGN fraction, since we are focusing on high-mass quiescent galaxies while excluding the strongest $24\mu\text{m}$ detections.

As noted in Aird et al. (2019), stellar mass-loss and AGN feedback tend to be disfavored mechanisms to cause relatively high-accretion rates and high AGN fractions in sub-MS and quiescent galaxies. The former could sustain the accretion onto the central BH by providing a relatively stable supply of low-angular momentum gas but is expected to result in relatively low accretion rates. Moreover, stellar mass loss is most efficient soon after star formation (2-5 Myr) and declines exponentially afterwards, making its contribution likely not sufficient to explain the highest λ_{EDD} measured for some of our objects (unless non-negligible SF is occurring). Instead, AGN feedback assumes that the gas supply, once used by the galaxy to sustain SF, is accreted by the central SMBH. However, even the shortest ages shown by our stellar populations would imply a stability of the radiatively efficient AGN feedback of order of hundreds of Myr, whereas radiatively efficient accretion is expected to be stable on time-scales of 0.1 Myr. One other mechanism proposed by Aird et al. 2019 could be the build-up of a compact bulge, which would increase the stellar density of the host galaxy, hence increasing the rate at which the AGN is triggered by infalling gas, as also supported by observations Barro et al. (2013). Fig. 14 shows that our likely-AGN hosts are among the most compact ones in the sample however they also show the lowest Sersic indices ($n=1.6\text{--}2.6$) implying that no clear-cut connection between radiative AGN feedback and central stellar density can be established with the present sample. However, despite no significant correlation being found between morphology (either R_e or n) and t_{50} , the very young mass weighted ages found for the sample as a whole and the average bulge dominated morphology suggest that structural transformation precedes or, at least, goes hand-in-hand with star formation rate suppression. The 30-40% fraction of AGN tentatively associated with young objects (seen also young quiescent galaxies in Schreiber et al. (2018)) might suggest that episodic AGN feedback might be triggered before a completely passive stellar core is settled.

9. Discussion

In the present paper we have characterized one of the largest representative samples of 10 high- z quiescent galaxies in terms of spectroscopic confirmation and age-estimation. We showed how HST observations are able to probe the (H-band) brightest end

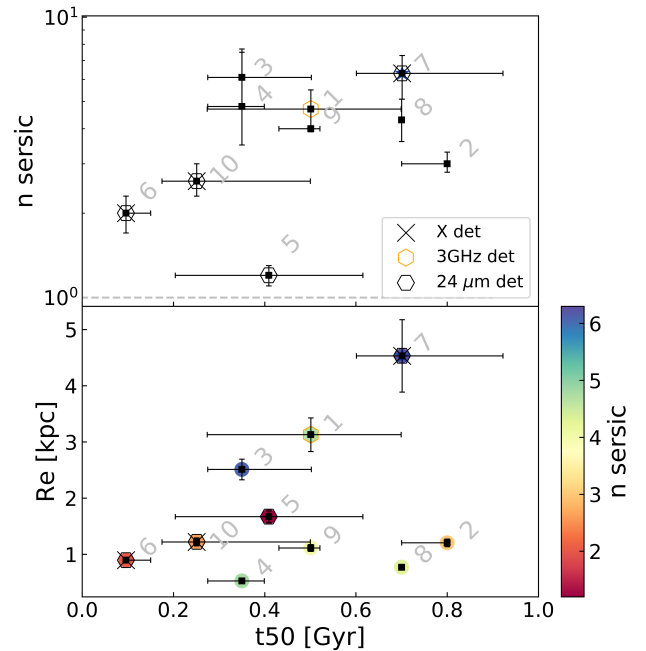


Fig. 14: Comparison between our mass-weighted ages and the morphological parameters derived in Lustig et al. (2020), namely Sersic index n and effective radius R_e at 5000 \AA rest-frame.

of the massive QG population providing access to clear spectral breaks in the majority of the objects. Such breaks can be used to quantitatively compare the amplitude of the Balmer absorption lines with respect to metal lines, hence quantifying the light-weighted contribution of young versus old stars at fixed stellar mass in early QGs. In other words, with relatively few HST orbits it is possible to both perform spectroscopic confirmation of QGs up to $z \sim 3.2$ and start quantifying the incidence of newly-quenched objects within the population. The particular configuration of spectral breaks characterising our sample (strong D_B and weak D_n4000) is due to the presence of luminous A-type stars. These often flag a relatively recent shut down of star formation, yet they have been also linked to galaxies hosting substantial amounts of obscured star formation contaminating the rest-frame colors commonly used when selecting high- z quiescent galaxies (Poggianti & Wu 2000; Lemaux et al. 2017). The quiescence of our targets was first tested and confirmed through their combined spectral (rest-frame NUV/optical) and photometric (rest-frame UV-to-NIR) emission, rejecting the presence of catastrophic photometric errors or prominent emission lines. They are however consistent with very young mass-weighted ages, which makes their final interpretation less clear. Given the shallow upper-limits on the obscured SFR placed by the current Spitzer/MIPS and Herschel/PACS and SPIRE data, we relied on the mean-stacked shallow detection at 3 GHz to constrain the potential obscured SFR to be on average below $50\text{ M}_{\odot}\text{ yr}^{-1}$ (D'Eugenio et al. 2020), hence 6 times lower the co-eval MS, at most. The individual $24\mu\text{m}$ flux densities of three $5\text{--}10\sigma$ detections in the J18 super-deblended catalog were converted to hard X-ray luminosities, compared to Chandra COSMOS Legacy X-ray detections and judged being consistent with being AGN-powered. Converting individual 3 GHz 3σ upper-limits into SFRs results in $<120\text{--}190\text{ M}_{\odot}\text{ yr}^{-1}$, which are not conclusive to exclude substantial obscured star formation on a galaxy-by-galaxy basis. We also note that the origin of the mid-

IR emission is in principle unclear since it can arise from multiple phenomena such as a dusty AGN torus, star-formation, hot circumstellar dust around AGB stars and/or the presence of diffuse cirrus clouds heated by hot stellar populations (Fumagalli et al. 2014) or a combination thereof. From the broad agreement between the prominent Balmer breaks and the mass weighted ages of our galaxies we conclude that they have quenched relatively recently prior to observation. However, dedicated mm observations are required for 40% of our objects to conclusively assess the level of residual star formation. These, in fact, could potentially represent examples of rapidly transitioning galaxies which underwent a sharp truncation of their star formation, possibly through AGN feedback.

9.1. The emergence of massive quiescent galaxies at high- z

Despite the overall stability of the spectral fitting mentioned above, one should keep in mind that age estimates still rely upon the spectral fitting scheme adopted, on the assumptions made in the choice of template libraries and ultimately on the shape of the SFH used. Keeping such caveats in mind, we can start making meaningful statements on the ages of our QGs through relative comparisons of the mass-weighted ages within our sample. The bulk of our targets is consistent with having suppressed their star-formation very recently, between 300-800 Myr prior to observation. The median value being 0.5 Gyr with a dispersion of 0.2 Gyr. Two outliers are present, ID 6 and ID 10, showing younger ages than the bulk of the sample, 0.1 and 0.25 Gyr respectively. Despite the fact that for ID 10 the D_B/D_n4000 ratio appears to be the strongest (hence pointing at the highest contribution of A-type stars with respect to the underlying stellar population), the S/N of our spectra prevents us from identifying significant differences among our galaxies. Moreover, the downward trend of the D_B/D_n4000 ratio at $t_{50} \leq 0.1$ Gyr precludes the possibility of testing the age inferred from the spectral fit, such as for ID 6. Assuming an exponentially declining SFH and our best-fit t_{50} , our galaxies are consistent with having been forming half of their stellar mass around $z_{\text{form}} \sim 3.5$ at $\text{SFR} \sim 1800\text{-}3000 M_{\odot} \text{ yr}^{-1}$, similarly to what reported in Valentino et al. (2020) but shifted at a later epoch. We caution, however, that such simple representations of SFHs are unlikely to be representative of the *peak* SFR if the true SFH was more complex, such as in the case of multiple phases in the SFR (Barro et al. 2016) or mergers (which imply a degeneracy with mass assembly, hence in lower SFRs split between the progenitors). Interestingly, the common selection of high- z QGs preferentially selects bright blue UVJ quiescent objects where "dust-poor" PSBs often lie. In some cases, it extends to a bluer region outside the standard quiescent boundaries (either in the UVJ or in the NUVrJ selection) where compact transitioning galaxies are thought to lie along their fast drop in SFR (Belli et al. 2019; Schreiber et al. 2018; Valentino et al. 2020; Forrest et al. 2020a). This implies that high- z quiescent galaxies are selected more or less in the same evolutionary phase, namely after O and B stars exited the Turn Off and before the same happens for A-type stars. This appears to be manifesting through similar distributions of (mass-weighted) ages among the highest- z samples (perhaps unsurprisingly, see Fig. 15). This also means that the magnitude cut necessary for spectral acquisition is biasing the selection of high- z QGs against dusty PSBs or galaxies more slowly transitioning into quiescence (Belli et al. 2019). Moreover, considering the cosmic time between $z=2.8$ and $z=1.8$, the mass-weighted ages inferred for our targets appear to be broadly consistent with passive evolution into old QGs at intermediate redshifts (Whitaker et al. 2013). This is not the

case for higher- z massive QGs, confirming that the high- z selection is directly probing the continuous injection of new compact quiescent galaxies into the passive population.

The enhanced fraction of PSBs (60%-70%, D'Eugenio et al. 2020; Lustig et al. 2020) among photometrically selected $\log(M_{\star}/M_{\odot}) \geq 11$ QGs at $z \sim 3$, is linked to the progressive migration of the red-sequence towards bluer colors with increasing redshift. PSBs represent an increasing fraction of the whole QGs population with redshift (Wild et al. 2016). Particularly so also because the transition from Balmer to CaII absorption lines is fast compared to the overall lifetime of a galaxy at low redshift (at the epochs spanned in this work, instead, such a phase naturally represents a much larger fraction of a galaxy lifetime). When considering the growth of the red sequence, the observed fraction of PSBs among massive QGs remains low <1-3% from $z=0$ to $z \sim 0.5$ (Tran et al. 2003) and fastens between $z \sim 1-2$ to $\sim 20\%$ -50%, with percentage variations mirroring different selection criteria (Le Borgne et al. 2006; Whitaker et al. 2013; Wild et al. 2016). The mounting fraction of massive QGs with evidence of recent quenching already accounts for half of the population at $z \sim 2$, when their number densities start to match (Whitaker et al. 2012). This is further supported by the growth rate of $\log(M_{\star}/M_{\odot}) \geq 10.8$ PSBs of less than 1 Gyr at $z \sim 2$ which accounts for half that of the whole quiescent population (Belli et al. 2019). The decrease in cosmic time allows to study the width of the distribution in quenching times of QGs: the emerging picture is one in which a continuous injection of objects into the quenched population manifests into the fast increase in the number density of young quiescent galaxies starting at $z \sim 1.5-2$ (Whitaker et al. 2011, 2013) with a reversal of their relative contribution to the red sequence with respect to old galaxies by $z \sim 3$. This trend appears to continue towards higher redshifts where relatively old quiescent galaxies appear to be still unobserved (Forrest et al. 2020b; Marsan et al. 2020). The latest spectroscopic constraints at $z \sim 3.5$ appear to find quasars or star forming redshift interlopers among the reddest objects in the passive UVJ region, however the long integrations required limit both the number and the quality of such spectra (Forrest et al. 2020b). At the time being, the question of whether or not PSBs scatter also into the reddest area of the passive UVJ region⁷ due to photometric errors or intrinsic properties such as dust or metallicity (which can also be read as *is the $z \sim 3$ population missing the descendants of any $z \sim 4-5$ massive quiescent galaxies?*) can be addressed only with very expensive targeted observations. The enhanced sensitivity of JWST will be able to map the full distribution of PSBs on the UVJ diagram to the highest redshifts. Establishing a detailed demographics of $z \sim 3$ (or higher) QGs to the faintest magnitudes will help clarifying the distribution of dust attenuation among spectroscopically confirmed extremely red-objects and in turn provide insights on the global star formation history of high- z QGs.

10. Summary and conclusions

We have obtained HST WFC3/G141 grism spectra for one of the first representative samples of ten $\log(M_{\star}/M_{\odot}) > 10.8$ quiescent galaxies at high redshift ($2.4 < z < 3.2$). HST observations efficiently provided us with the largest sample of QGs with a full continuous coverage along the Balmer/4000 Å spectral region at these redshifts. This allowed us to perform spectroscopic confirmation of QGs up to $z \sim 3.2$ and, thanks to widespread prominent Balmer Breaks, we were able to start quantifying the inci-

⁷ E.g. (U-V)+(V-J)>2.8

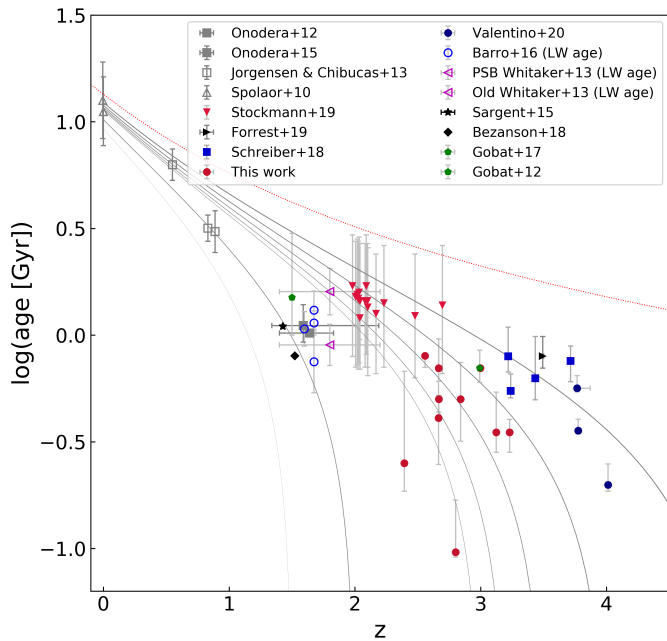


Fig. 15: Age evolution with redshift in $\log(M_*/M_\odot) > 10.5$ quiescent galaxies. Adapted from Onodera et al. (2015). For $z > 2.5$ QGs we show their mass-weighted ages (t_{50s}). The four targets selected from Schreiber et al. (2018) correspond to those recently followed up by Esdaile et al. (2020). Gray solid lines show, from thin to thick, the age of simple stellar populations made at a z_{form} from 1.5 to 5. The red dotted line marks the age of the Universe as a function of redshift.

dence of newly-quenched objects within the massive quenched population against contamination by lower redshift interlopers. The quiescence of our targets was tested by means of the combined information of our newly acquired rest-frame NUV/optical spectra and COSMOS2015 UV-to-NIR photometry. In addition, we also considered mid-IR, far-IR and radio detections from recently released super-deblended photometry (Jin et al. 2018).

Our main conclusions can be summarized as follows:

- successful spectroscopic confirmation was achieved for the full sample, confirming the quality of the original photometric selection;
- the joint analysis of our newly acquired rest-frame NUV/optical spectra and COSMOS2015 broad-band UV-to-NIR photometry confirms the quiescent nature of all our targets;
- although IR-based constraints on the obscured SFRs of our individual targets are weak with the available data ($< 120\text{--}190 M_\odot \text{ yr}^{-1}$), the quiescent nature inferred from grism spectra and optical/NIR SEDs is globally supported from the 3GHz stack of the sample yielding an obscured SFR $< 50 M_\odot \text{ yr}^{-1}$ (D'Eugenio et al. 2020);
- the use of photometric Zero Points re-calibrations proposed in Laigle et al. (2016) appears to be disfavored by our data. Such corrections were derived on a set of spectroscopically confirmed quiescent among a much larger number of star forming galaxies at intermediate redshifts and might not be necessary when it comes to extract the SEDs of QGs at high- z ;
- an attenuation curve steeper than Calzetti tends to reduce tensions between age and dust extinction values between photometry and spectroscopy. Nonetheless, our data do not allow

to securely discriminate among attenuation curves of different slopes;

- marginalizing the spectro-photometric fit over different attenuation curves and SFHs, the typical mass-weighted ages inferred for our objects range from 300–800 Myr, pointing at a recent rapid suppression of their SFR. Their global strength was quantified and compared to the one of the 4000 Å break by means of the D_B/D_n4000 ratio which is systematically higher than 1. This spectroscopically confirms on a galaxy-by-galaxy basis the post-SB nature of massive bright QGs, already pointed out by means of stacking (D'Eugenio et al. 2020) and by individual high-resolution spectra (Forrest et al. 2020b). More observational efforts are required to explore to which extent strong Balmer absorption lines are spread among lower mass-to-light ratio objects;
- interpreting our mid-IR and X-ray individual detections and the radio-stack shallow detection as a signature of AGN activity, our results are consistent with: a widespread radio AGN activity a factor of 4 stronger than in similarly massive QGs at intermediate redshifts, and a 30–40% incidence of luminous AGN in which the BH mass growth is substantially enhanced with respect both to $z \sim 2$ quiescent analogs ($\times 30$) and to coeval star forming galaxies at the same stellar mass ($\times 60$). This is in agreement with the recent results of Carraro et al. (2020) on the stacked emission of photometrically selected populations of QGs at $2.25 < z < 3.50$;
- our galaxies are globally characterized by a bulge-dominated, compact morphology (Lustig et al. 2020). Despite no clear trend between mass-weighted ages and R_e or Sérsic indices could be found within the sample, the young ages yielded by their grism spectra and broad-band photometry suggest that structural transformation may precede or be concomitant with quenching.

The fast evolutionary phase probed by the magnitude-limited color selection seems the one in which the majority of $z > 2.5$ QGs are caught, systematically selecting newly quenched(-ing) objects which enter the quiescent population. We expect the number density of spectroscopically confirmed post-SBs (which was already matching the one of old systems at $z \sim 2$ based on photometric selections (Whitaker et al. 2013) to fully dominate the QGs mass-function at $z \sim 3$. JWST and ALMA will be crucial to trace the full demographics the quiescent population in an effort to map the distribution in quenching times and dust/molecular gas content, i.e. to get further insights on the global SFH of the emerging massive quenched systems.

Acknowledgements. We are grateful to G. Brammer for assistance with the data reduction, to C. Vignali for providing X-ray spectra and M. Salvato for additional redshift constraints and helpful discussions. C.D. is grateful to C. Gomez-Guijarro for helpful discussions. V.S. acknowledges support from the ERC-StG ClustersXCosmo grant agreement 716762. I.D. acknowledges the European Union's Horizon 2020 research and innovation program under the Marie Skłodowska-Curie grant agreement No 788679. A.C. acknowledges the support from the grants PRIN-MIUR 2017 and ASI n.2018-23-HH.0. Based on data products from observations made with ESO Telescopes at the La Silla Paranal Observatory under ESO programme ID 179.A-2005 and on data products produced by TERAPIX and the Cambridge Astronomy Survey Unit on behalf of the UltraVISTA consortium (Laigle cat.).

ID	z_{spec}	$\log(M_*/M_\odot)$	t_{50} [Gyr]	A_V [mag]	δ	DB	D_n4000	$f_{24\mu\text{m}}$ [mJy]	$\log L_X$ obs.	$\log L_X$ 24 μm	$S_{3\text{GHz}}$ [mJy]	$\text{SFR}_{24\mu\text{m}}$ [$M_\odot \text{yr}^{-1}$]	$\text{SFR}_{3\text{GHz}}$ [$M_\odot \text{yr}^{-1}$]
1	$2.841^{+0.021}_{-0.018}$	11.37	$0.5^{+0.2}_{-0.2}$	$0.2^{+0.3}_{-0.1}$	[-0.7,0]	2.22 ± 0.51	1.47 ± 0.23	-	< 43.6	-	0.576 ± 0.03	867	~ 12930
2	$2.557^{+0.005}_{-0.005}$	11.50	$0.8^{+0.0}_{-0.1}$	$0.1^{+0.1}_{-0.0}$	[-0.4,0]	2.02 ± 0.22	1.34 ± 0.10	-	< 43.16	-	-	-	-
3	$3.124^{+0.003}_{-0.003}$	11.55	$0.4^{+0.2}_{-0.1}$	$0.4^{+0.2}_{-0.2}$	[-0.7,0]	2.39 ± 0.19	1.37 ± 0.11	0.041 ± 0.018	< 43.6	43.73	0.011 ± 0.004	< 540	< 307
4	$3.230^{+0.007}_{-0.006}$	10.98	$0.4^{+0.1}_{-0.1}$	$0.1^{+0.1}_{-0.0}$	[-0.7,-0.4]	3.15 ± 0.48	1.21 ± 0.09	0.000 ± 0.024	< 43.6	43.60	0.003 ± 0.003	< 967	< 242
5	$2.665^{+0.003}_{-0.007}$	11.34	$0.4^{+0.2}_{-0.2}$	$0.8^{+0.2}_{-0.2}$	[-0.4]	2.18 ± 0.29	1.39 ± 0.12	0.171 ± 0.017	< 43.6	44.02	0.000 ± 0.002	644	< 122
6	$2.801^{+0.005}_{-0.002}$	11.36	$0.1^{+0.1}_{-0.0}$	$1.0^{+0.0}_{-0.1}$	[-0.4]	2.02 ± 0.27	1.34 ± 0.12	0.100 ± 0.021	44.34 ± 0.32	43.91	0.002 ± 0.003	508	< 197
7	$2.674^{+0.005a}_{-0.009}$	11.55	$0.7^{+0.2}_{-0.1}$	$0.6^{+0.1}_{-0.2}$	[-0.7,0]	2.02 ± 0.35	1.27 ± 0.17	0.111 ± 0.011	44.26 ± 0.36	43.89	0.004 ± 0.003	419	< 183
8	$2.998^{+0.002}_{-0.003}$	11.40	$0.7^{+0.0}_{-0.0}$	$0.1^{+0.0}_{-0.0}$	[-0.7,-0.4]	2.23 ± 0.2	1.41 ± 0.09	0.000 ± 0.018	< 43.6	43.42	0.002 ± 0.002	< 394	< 144
9	$2.667^{+0.015}_{-0.002}$	11.53	$0.5^{+0.0}_{-0.1}$	$0.7^{+0.1}_{-0.0}$	[-0.4,0]	2.07 ± 0.41	1.61 ± 0.20	0.032 ± 0.023	< 43.6	43.50	0.005 ± 0.003	< 261	< 183
10	$2.393^{+0.011}_{-0.000}$	11.33	$0.3^{+0.3}_{-0.1}$	$1.6^{+0.1}_{-0.3}$	[0]	2.25 ± 0.51	1.15 ± 0.15	0.146 ± 0.020	43.73 ± 0.29	43.87	0.005 ± 0.003	289	< 155

^a Obtained with the addition of NUV-to-NIR broad-band photometry as described in Sect. 4.2.

Table 3: Best fit values and their 1σ uncertainties. Observed 24 μm and 3GHz flux densities. Upper limits are given at 3σ . Those for the observed bolometric X-ray luminosities were derived median-stacking all undetected sources. Stellar masses are taken from Lustig et al. 2020 and converted to a Salpeter IMF. ID 2 is absent from the J18 catalog due to the absence of K_s and VLA 3 GHz radio priors.

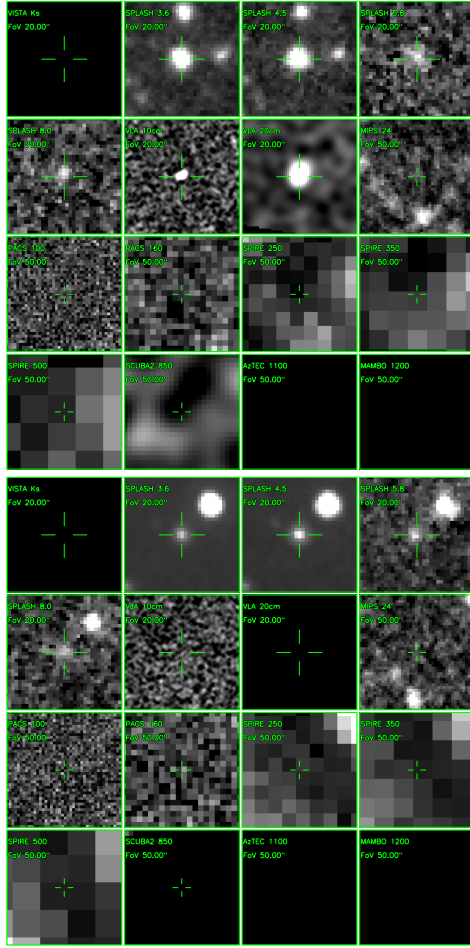
References

- Aird, J., Coil, A. L., & Georgakakis, A. 2019, MNRAS, 484, 4360
Anders, P. & Fritze-v. Alvensleben, U. 2003, A&A, 401, 1063
Arnouts, S., Walcher, C. J., Le Fèvre, O., et al. 2007, A&A, 476, 137
Avni, Y. 1976, ApJ, 210, 642
Baldry, I. K., Glazebrook, K., Brinkmann, J., et al. 2004, ApJ, 600, 681
Balogh, M. L., Morris, S. L., Yee, H. K. C., Carlberg, R. G., & Ellingson, E. 1999, ApJ, 527, 54
Barro, G., Faber, S. M., Dekel, A., et al. 2016, ApJ, 820, 120
Barro, G., Faber, S. M., Pérez-González, P. G., et al. 2013, ApJ, 765, 104
Belli, S., Newman, A. B., & Ellis, R. S. 2015, ApJ, 799, 206
Belli, S., Newman, A. B., & Ellis, R. S. 2017, ApJ, 834, 18
Belli, S., Newman, A. B., & Ellis, R. S. 2019, ApJ, 874, 17
Best, P. N., Kauffmann, G., Heckman, T. M., et al. 2005, MNRAS, 362, 25
Béthermin, M., Daddi, E., Magdis, G., et al. 2015, A&A, 573, A113
Bezanson, R., van Dokkum, P., van de Sande, J., Franx, M., & Kriek, M. 2013, ApJ, 764, L8
Brammer, G., Ryan, R., & Pirzkal, N. 2015, Source-dependent master sky images for the WFC3/IR grisms, Space Telescope WFC Instrument Science Report
Brammer, G. B., van Dokkum, P. G., & Coppi, P. 2008, ApJ, 686, 1503
Bruzual, G. & Charlot, S. 2003, MNRAS, 344, 1000
Calzetti, D., Armus, L., Bohlin, R. C., et al. 2000, ApJ, 533, 682
Capozzi, D., Maraston, C., Daddi, E., et al. 2016, MNRAS, 456, 790
Carollo, C. M., Bschorr, T. J., Renzini, A., et al. 2013, ApJ, 773, 112
Carraro, R., Rodighiero, G., Cassata, P., et al. 2020, arXiv e-prints, arXiv:2007.11002
Cattaneo, A., Dekel, A., Devriendt, J., Guiderdoni, B., & Blaizot, J. 2006, MNRAS, 370, 1651
Cecchi, R., Bolzonella, M., Cimatti, A., & Girelli, G. 2019, ApJ, 880, L14
Cimatti, A., Cassata, P., Pozzetti, L., et al. 2008, A&A, 482, 21
Cimatti, A., Daddi, E., & Renzini, A. 2006, A&A, 453, L29
Cimatti, A., Daddi, E., Renzini, A., et al. 2004, Nature, 430, 184
Citro, A., Pozzetti, L., Moresco, M., & Cimatti, A. 2016, A&A, 592, A19
Civano, F., Marchesi, S., Comastri, A., et al. 2016, ApJ, 819, 62
Croton, D. J., Springel, V., White, S. D. M., et al. 2006, MNRAS, 365, 11
Daddi, E., Bournaud, F., Walter, F., et al. 2010, ApJ, 713, 686
Daddi, E., Cimatti, A., Renzini, A., et al. 2004, ApJ, 617, 746
Daddi, E., Renzini, A., Pirzkal, N., et al. 2005, ApJ, 626, 680
Davé, R., Anglés-Alcázar, D., Narayanan, D., et al. 2019, MNRAS, 486, 2827
Davé, R., Thompson, R., & Hopkins, P. F. 2016, MNRAS, 462, 3265
Davidzon, I., Ilbert, O., Laigle, C., et al. 2017, A&A, 605, A70
De Lucia, G. & Blaizot, J. 2007, MNRAS, 375, 2
Dekel, A. & Birnboim, Y. 2006, MNRAS, 368, 2
Dekel, A., Sari, R., & Ceverino, D. 2009, ApJ, 703, 785
Dekel, A. & Silk, J. 1986, ApJ, 303, 39
Delhaize, J., Smolčić, V., Delvecchio, I., et al. 2017, A&A, 602, A4
Delvecchio, I., Daddi, E., Sargent, M. T., et al. 2020, arXiv e-prints, arXiv:2010.05510
D'Eugenio, C., Daddi, E., Gobat, R., et al. 2020, ApJ, 892, L2
Di Matteo, T., Springel, V., & Hernquist, L. 2005, Nature, 433, 604
Draine, B. T. & Li, A. 2007, ApJ, 657, 810
Drory, N., Bundy, K., Leauthaud, A., et al. 2009, ApJ, 707, 1595
Dunlop, J., Peacock, J., Spinrad, H., et al. 1996, Nature, 381, 581
Elbaz, D., Leiton, R., Nagar, N., et al. 2018, A&A, 616, A110
Emsellem, E., Cappellari, M., Krajnović, D., et al. 2011, MNRAS, 414, 888
Esdaile, J., Glazebrook, K., Labbe, I., et al. 2020, arXiv e-prints, arXiv:2010.09738
Estrada-Carpenter, V., Papovich, C., Momcheva, I., et al. 2019, ApJ, 870, 133
Estrada-Carpenter, V., Papovich, C., Momcheva, I., et al. 2020, ApJ, 898, 171
Feldmann, R. & Mayer, L. 2015, MNRAS, 446, 1939
Fiore, F., Puccetti, S., Brusa, M., et al. 2009, ApJ, 693, 447
Fitzpatrick, E. L. & Massa, D. 1986, ApJ, 307, 286
Fontana, A., Pozzetti, L., Donnarumma, I., et al. 2004, A&A, 424, 23
Forrest, B., Annunziatella, M., Wilson, G., et al. 2020a, ApJ, 890, L1
Forrest, B., Marsan, Z. C., Annunziatella, M., et al. 2020b, arXiv e-prints, arXiv:2009.07281
Franx, M., Labbé, I., Rudnick, G., et al. 2003, ApJ, 587, L79
Fumagalli, M., Labbé, I., Patel, S. G., et al. 2014, ApJ, 796, 35
Gallazzi, A., Charlot, S., Brinchmann, J., White, S. D. M., & Tremonti, C. A. 2005, MNRAS, 362, 41
Gargiulo, A., Saracco, P., Tamburri, S., Lonoce, I., & Ciocca, F. 2016, A&A, 592, A132
Genel, S., Vogelsberger, M., Springel, V., et al. 2014, MNRAS, 445, 175
Genzel, R., Tacconi, L. J., Gracia-Carpio, J., et al. 2010, MNRAS, 407, 2091
Gilli, R., Comastri, A., & Hasinger, G. 2007, A&A, 463, 79
Girelli, G., Pozzetti, L., Bolzonella, M., et al. 2020, A&A, 634, A135
Glazebrook, K., Schreiber, C., Labbé, I., et al. 2017, Nature, 544, 71
Gobat, R., Daddi, E., Magdis, G., et al. 2018, Nature Astronomy, 2, 239
Gobat, R., Daddi, E., Strazzullo, V., et al. 2017, A&A, 599, A95

- Gobat, R., Strazzullo, V., Daddi, E., et al. 2012, *ApJ*, 759, L44
- Gómez-Guijarro, C., Magdis, G. E., Valentino, F., et al. 2019, *ApJ*, 886, 88
- Gómez-Guijarro, C., Toft, S., Karim, A., et al. 2018, *ApJ*, 856, 121
- Häring, N. & Rix, H.-W. 2004, *ApJ*, 604, L89
- Henriques, B. M. B., White, S. D. M., Thomas, P. A., et al. 2017, *MNRAS*, 469, 2626
- Hopkins, P. F., Hernquist, L., Cox, T. J., et al. 2006, *ApJS*, 163, 1
- Ilbert, O., McCracken, H. J., Le Fèvre, O., et al. 2013, *A&A*, 556, A55
- Jin, S., Daddi, E., Liu, D., et al. 2018, *ApJ*, 864, 56
- Johansson, P. H., Naab, T., & Ostriker, J. P. 2009, *ApJ*, 697, L38
- Johansson, P. H., Naab, T., & Ostriker, J. P. 2012, *ApJ*, 754, 115
- Kawinwanichakij, L., Papovich, C., Ciardullo, R., et al. 2020, *ApJ*, 892, 7
- Kennicutt, Robert C., J. 1998, *ARA&A*, 36, 189
- Khochfar, S. & Ostriker, J. P. 2008, *ApJ*, 680, 54
- Kriek, M. & Conroy, C. 2013, *ApJ*, 775, L16
- Kriek, M., Conroy, C., van Dokkum, P. G., et al. 2016, *Nature*, 540, 248
- Kriek, M., van Dokkum, P. G., Franx, M., et al. 2006, *ApJ*, 645, 44
- Kriek, M., van Dokkum, P. G., Labbé, I., et al. 2009, *ApJ*, 700, 221
- Krogager, J. K., Zirm, A. W., Toft, S., Man, A., & Brammer, G. 2014, *ApJ*, 797, 17
- Labbé, I., Huang, J., Franx, M., et al. 2005, *ApJ*, 624, L81
- Laigle, C., McCracken, H. J., Ilbert, O., et al. 2016, *ApJS*, 224, 24
- Le Borgne, D., Abraham, R., Daniel, K., et al. 2006, *ApJ*, 642, 48
- Le Floch, E., Aussel, H., Ilbert, O., et al. 2009, *ApJ*, 703, 222
- Lemaux, B. C., Le Floch, E., Le Fèvre, O., et al. 2017, *A&A*, 597, C1
- Liu, D., Daddi, E., Dickinson, M., et al. 2018, *ApJ*, 853, 172
- Lusso, E., Comastri, A., Simons, B. D., et al. 2012, *MNRAS*, 425, 623
- Lustig, P., Strazzullo, V., DEugenio, C., et al. 2020, *MNRAS*
- Madau, P. & Dickinson, M. 2014, *ARA&A*, 52, 415
- Magdis, G. E., Daddi, E., Béthermin, M., et al. 2012, *ApJ*, 760, 6
- Magnelli, B., Ivison, R. J., Lutz, D., et al. 2015, *A&A*, 573, A45
- Maltby, D. T., Almaini, O., Wild, V., et al. 2018, *MNRAS*, 480, 381
- Man, A. & Belli, S. 2018, *Nature Astronomy*, 2, 695
- Marsan, Z. C., Muzzin, A., Marchesini, D., et al. 2020, *arXiv e-prints*, arXiv:2010.04725
- Martig, M., Bournaud, F., Teyssier, R., & Dekel, A. 2009, *ApJ*, 707, 250
- Matharu, J., Muzzin, A., Brammer, G. B., et al. 2019, *MNRAS*, 484, 595
- McCarthy, I. G., Schaye, J., Bower, R. G., et al. 2011, *MNRAS*, 412, 1965
- McCracken, H. J., Capak, P., Salvato, M., et al. 2010, *ApJ*, 708, 202
- Merlin, E., Fortuni, F., Torelli, M., et al. 2019, *MNRAS*, 490, 3309
- Mullaney, J. R., Alexander, D. M., Goulding, A. D., & Hickox, R. C. 2011, *MNRAS*, 414, 1082
- Murray, N., Quataert, E., & Thompson, T. A. 2005, *ApJ*, 618, 569
- Muzzin, A., Marchesini, D., Stefanon, M., et al. 2013, *ApJ*, 777, 18
- Nelson, D., Genel, S., Vogelsberger, M., et al. 2015, *MNRAS*, 448, 59
- Nelson, D., Springel, V., Pillepich, A., et al. 2019, *Computational Astrophysics and Cosmology*, 6, 2
- Newman, A. B., Belli, S., Ellis, R. S., & Patel, S. G. 2018, *ApJ*, 862, 125
- Newman, A. B., Ellis, R. S., Bundy, K., & Treu, T. 2012, *ApJ*, 746, 162
- Noll, S., Burgarella, D., Giovannoli, E., et al. 2009, *A&A*, 507, 1793
- Olsen, K. P., Rasmussen, J., Toft, S., & Zirm, A. W. 2013, *ApJ*, 764, 4
- Onodera, M., Carollo, C. M., Renzini, A., et al. 2015, *ApJ*, 808, 161
- Onodera, M., Renzini, A., Carollo, M., et al. 2012, *ApJ*, 755, 26
- Pillepich, A., Springel, V., Nelson, D., et al. 2018, *MNRAS*, 473, 4077
- Poggianti, B. M. & Wu, H. 2000, *ApJ*, 529, 157
- Pozzetti, L., Bolzonella, M., Zucca, E., et al. 2010, *A&A*, 523, A13
- Pozzetti, L. & Mannucci, F. 2000, *MNRAS*, 317, L17
- Puglisi, A., Daddi, E., Liu, D., et al. 2019, *ApJ*, 877, L23
- Renzini, A. 2006, *ARA&A*, 44, 141
- Salim, S., Boquien, M., & Lee, J. C. 2018, *ApJ*, 859, 11
- Salpeter, E. E. 1955, *ApJ*, 121, 161
- Sanders, D. B., Soifer, B. T., Elias, J. H., et al. 1988, *ApJ*, 325, 74
- Saracco, P., Longhetti, M., & Gargiulo, A. 2011, *MNRAS*, 412, 2707
- Sargent, M. T., Daddi, E., Béthermin, M., et al. 2014, *ApJ*, 793, 19
- Schaye, J., Crain, R. A., Bower, R. G., et al. 2015, *MNRAS*, 446, 521
- Schreiber, C., Glazebrook, K., Nanayakkara, T., et al. 2018, *A&A*, 618, A85
- Schreiber, C., Pannella, M., Elbaz, D., et al. 2015, *A&A*, 575, A74
- Smolčić, V., Novak, M., Bondi, M., et al. 2017, *A&A*, 602, A1
- Steinhardt, C. L., Capak, P., Masters, D., & Speagle, J. S. 2016, *ApJ*, 824, 21
- Stockmann, M., Toft, S., Gallazzi, A., et al. 2020, *ApJ*, 888, 4
- Straatman, C. M. S., Labbé, I., Spitler, L. R., et al. 2014, *ApJ*, 783, L14
- Strazzullo, V., Daddi, E., Gobat, R., et al. 2015, *A&A*, 576, L6
- Tacconi, L. J., Genzel, R., Neri, R., et al. 2010, *Nature*, 463, 781
- Thomas, D., Maraston, C., Bender, R., & Mendes de Oliveira, C. 2005, *ApJ*, 621, 673
- Thomas, D., Maraston, C., Schawinski, K., Sarzi, M., & Silk, J. 2010, *MNRAS*, 404, 1775
- Toft, S., Gallazzi, A., Zirm, A., et al. 2012, *ApJ*, 754, 3
- Toft, S., Smolčić, V., Magnelli, B., et al. 2014, *ApJ*, 782, 68
- Tran, K.-V. H., Franx, M., Illingworth, G., Kelson, D. D., & van Dokkum, P. 2003, *ApJ*, 599, 865
- Valentino, F., Tanaka, M., Davidzon, I., et al. 2020, *ApJ*, 889, 93
- van de Sande, J., Kriek, M., Franx, M., et al. 2013, *ApJ*, 771, 85
- van Dokkum, P. G., Bezanson, R., van der Wel, A., et al. 2014, *ApJ*, 791, 45
- van Dokkum, P. G., Franx, M., Kriek, M., et al. 2008, *ApJ*, 677, L5
- Vogelsberger, M., Genel, S., Springel, V., et al. 2014a, *Nature*, 509, 177
- Vogelsberger, M., Genel, S., Springel, V., et al. 2014b, *MNRAS*, 444, 1518
- Wellons, S., Torrey, P., Ma, C.-P., et al. 2015, *MNRAS*, 449, 361
- Whitaker, K. E., Kriek, M., van Dokkum, P. G., et al. 2012, *ApJ*, 745, 179
- Whitaker, K. E., Labbé, I., van Dokkum, P. G., et al. 2011, *ApJ*, 735, 86
- Whitaker, K. E., van Dokkum, P. G., Brammer, G., et al. 2013, *ApJ*, 770, L39
- Wild, V., Almaini, O., Dunlop, J., et al. 2016, *MNRAS*, 463, 832
- Williams, R. J., Quadri, R. F., Franx, M., van Dokkum, P., & Labbé, I. 2009, *ApJ*, 691, 1879
- Zolotov, A., Dekel, A., Mandelker, N., et al. 2015, *MNRAS*, 450, 2327

Appendix A: Additional plots

We here insert the multi-wavelength cutouts (from K_s -band to 20 cm) of our sources, together with their SED fits when available. SEDs for IDs 1 and 2 are not present since ID1 lies in a region subjected to unreliable IR fluxes and uncertainties, while ID 2 is not present in the J18 catalog due to lack of UltraVISTA K_s and VLA 3 GHz radio priors. SED fitting was carried out fixing the redshift to the best fitting grism value of each galaxy and includes four components: a stellar component from BC03 templates (black curve); a mid-IR AGN torus from Mullaney et al. 2011 (red curve); a dust continuum component from Magdis et al. 2012 templates including Béthermin et al. 2015 L_{IR}/M_{dust} evolution with redshift (green curve); and a power-law radio continuum (Magnelli et al. 2015; Delhaize et al. 2017). The downward arrows show the 2σ upper limit at a given wavelength.



ID 1
zspec=2.841
NO SED

ID 2
zspec=2.557
NO SED

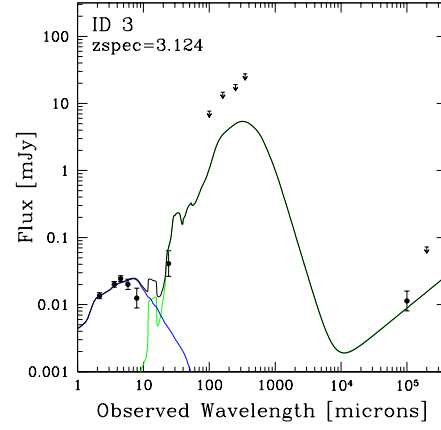
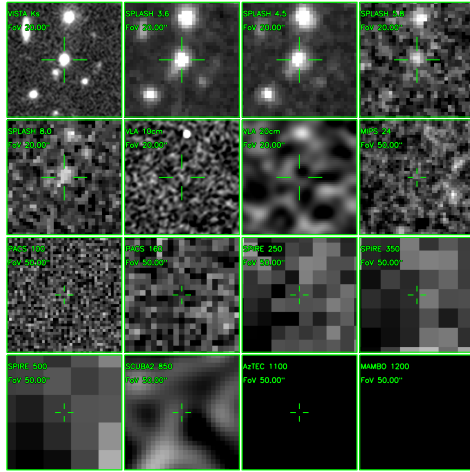
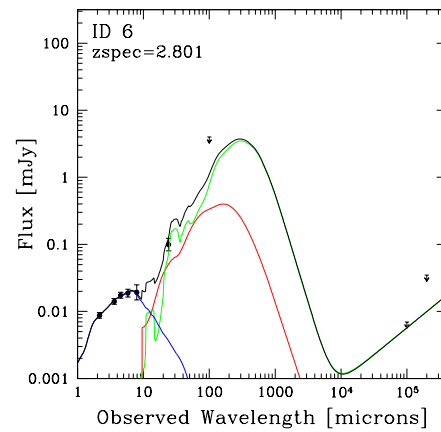
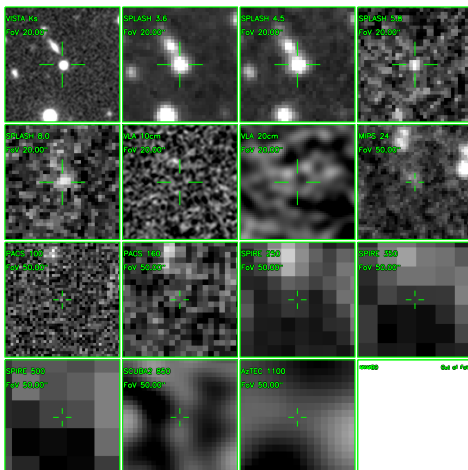
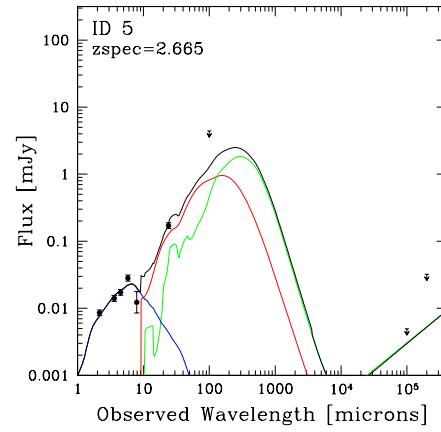
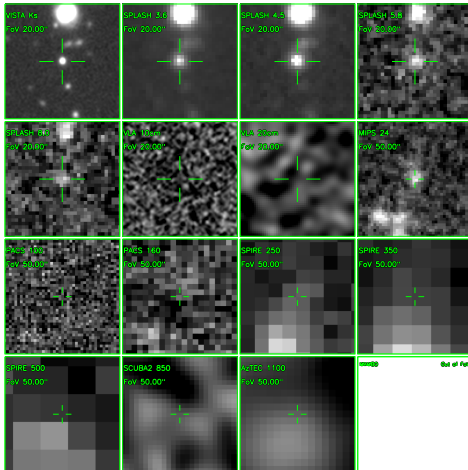
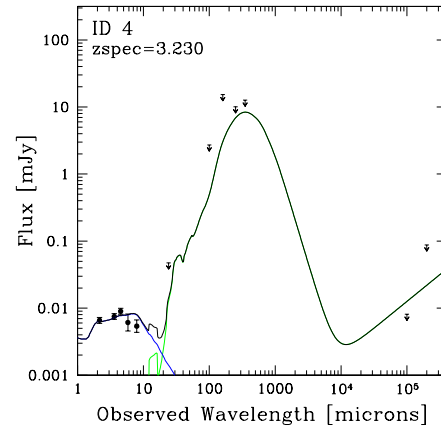
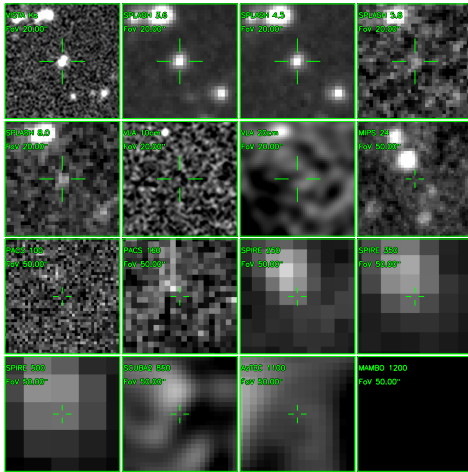


Fig. A.1: Left panel: multiband cutouts of our targets. The green text marks the instrument, the observed wavelength in units of μm and the size of the Field of View. Right panel: fits to the SEDs of our galaxies. The SEDs are fitted with a starburst-like dust continuum component (green curve Magdis et al. 2012), a stellar component (blue curve; Bruzual & Charlot 2003) and an AGN torus component (red curve Mullaney et al. 2011). The fits were fixed to the grism redshifts derived above. Upper limits are at 2σ .



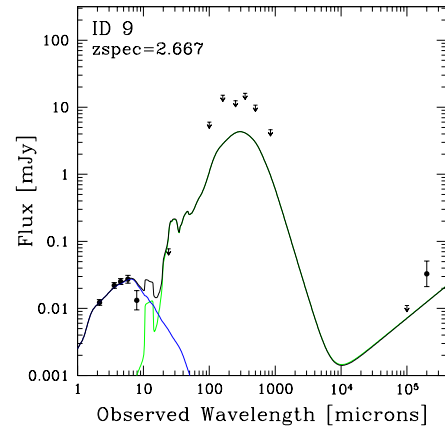
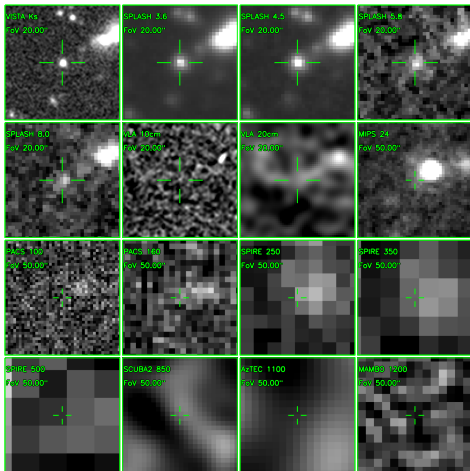
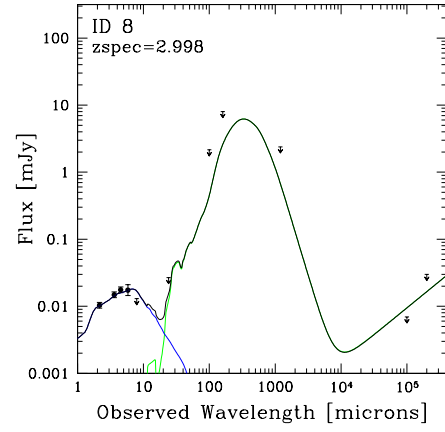
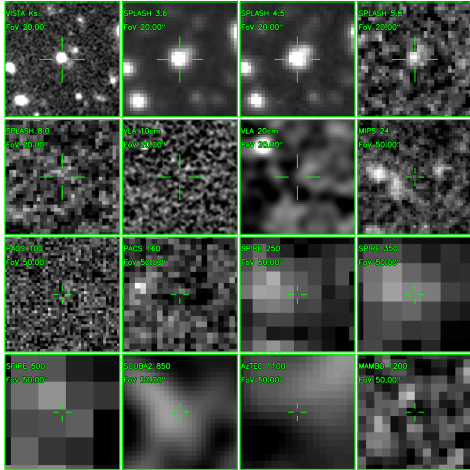
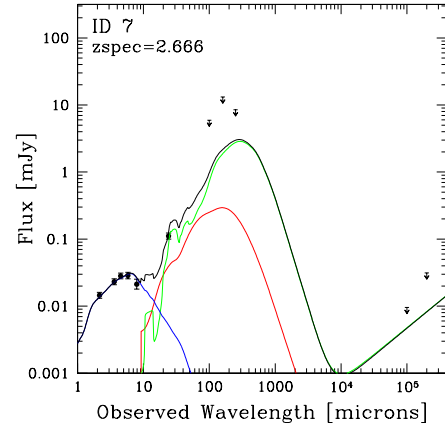
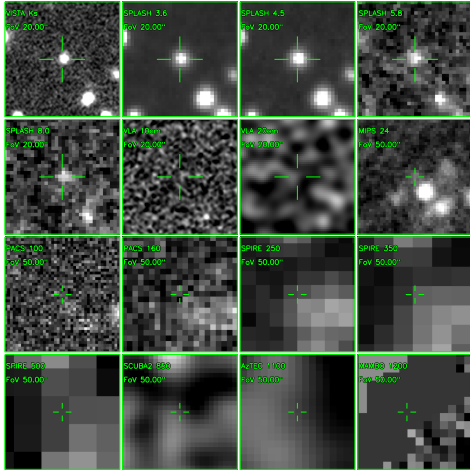


Fig. A.3: Continued.

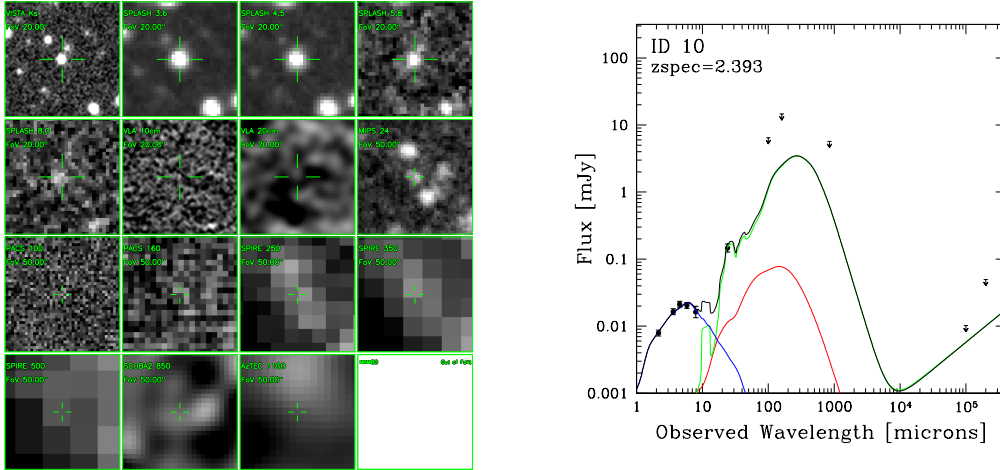


Fig. A.4: Continued.